Boreal Summer Extratropical Intraseasonal Waves over the Eurasian Continent and Real-Time Monitoring Metrics

Tao Zhu,[a] Jing Yang[orcid],[a,b] Bin Wang,[c] and Qing Bao[d]

[a] *State Key Laboratory of Earth Surface Processes and Resource Ecology/Key Laboratory of Environmental Change and Natural Disaster, Faculty of Geographical Science, Beijing Normal University, Beijing, China*
[b] *Faculty of Geographical Science, Beijing Normal University, Beijing, China*
[c] *Department of Atmospheric Sciences and International Pacific Research Center, University of Hawai'i at Mānoa, Honolulu, Hawaii*
[d] *State Key Laboratory of Numerical Modeling for Atmospheric Sciences and Geophysical Fluid Dynamics (LASG), Institute of Atmospheric Physics, Chinese Academy of Sciences, Beijing, China*

ABSTRACT: Boreal summer extratropical intraseasonal oscillation (EISO) is crucial in modulating regional subseasonal variation and particularly causing extreme meteorological events, but it has yet to be well clarified and operationally monitored. This study first objectively sorts out three dominant EISOs trapped along two extratropical westerly jet streams over Eurasia, and then proposes the corresponding real-time metrics. The three dominant EISOs are (i) an 8–25-day eastward-propagating wave along the subtropical westerly jet (EISO-SJE) initiating at the exit of the North America–North Atlantic jet and strengthening over the Black Sea–Caspian Sea–arid central Asia region; (ii) a 10–30-day eastward-traveling wave along the polar front jet (EISO-PJE), starting near Scandinavia and enhancing from the East European Plain to the West Siberian Plain and then decaying over the Okhotsk region; (iii) a 10–40-day westward-migrating wave along the polar front jet (EISO-PJW), which enhances near the Ural Mountains and weakens over Scandinavia. The real-time metrics then, following the three EISOs, have been constructed, and they are able to capture the spatiotemporal features of three EISOs in application. Moreover, the close linkages between these EISOs and the regional extremes/the blocking occurrence have been clearly demonstrated, confirming the importance of real-time EISO metrics. Together with tropical intraseasonal oscillation, this study provides the subseasonal-to-seasonal (S2S) community with a well-portrayed unified picture of extratropical intraseasonal waves and the real-time metrics for monitoring boreal summer intraseasonal signals over Eurasia and facilitate subseasonal predictions.

SIGNIFICANCE STATEMENT: Boreal summer extratropical intraseasonal oscillation (EISO) has drawn increasing attention owing to its importance in triggering extreme weather events and affecting regional subseasonal prediction. However, despite the urgent need of the subseasonal-to-seasonal (S2S) community, a comprehensive delineation of EISO diversity and real-time EISO monitoring remain the gap of knowledge. This study objectively sorts out and comprehensively clarifies three dominant EISOs trapped along two extratropical westerly jet streams over Eurasia. More importantly, the well-portrayed real-time EISO metrics are constructed based on three EISOs, which are applicable for operational real-time monitoring, subseasonal prediction, and model evaluation. This study stimulates an extratropical focus in the S2S community as a complementary component in addition to monitoring the MJO's teleconnection to the mid- to high latitudes.

---

1. Introduction

The intraseasonal oscillation (ISO) is one of the important atmospheric internal modes (Li 1991; Hoskins 2013). The tropical ISO has been well recognized and extensively documented since the pioneering work of Madden and Julian (1971, 1972), including an equatorial eastward-propagating oscillation [i.e., the Madden–Julian oscillation (MJO)] in boreal winter (e.g., Zhang 2005) and the prevailing meridionally (northeastward- and northwestward-) propagating ISO over the Asian monsoon regions in boreal summer (e.g., Wang and Xie 1997; Annamalai and Slingo 2001; Kemball-Cook and Wang 2001; Jiang et al. 2004; Yang et al. 2008; Wang et al. 2021). Since the tropical ISO significantly affects both tropical and extratropical weather and climate (Hendon and Liebmann 1990; Liebmann et al. 1994; Maloney and Hartmann 2000; Sultan et al. 2003), several effective indices have been well-constructed for the real-time monitoring and subseasonal prediction of tropical ISO, including the MJO (Wheeler and Hendon 2004) index, boreal summer ISO (BSISO) index (Lee et al. 2013), and quasi-biweekly oscillation index (Qian et al. 2019). Currently, these tropical ISO indices are widely used in

operational services (e.g., http://www.bom.gov.au/climate/mjo/; https://apcc21.org/ser/).

Compared with tropical ISO, extratropical intraseasonal oscillation (EISO) has been less well studied, especially in boreal summer. EISO was first recognized in the "index cycle" with a period of 4–6 weeks in boreal winter (Namias 1950), and since then, considerable attention has been given to the boreal winter EISO. For instance, a quasi-23-day westward-propagating wave across North America was reported (Branstator 1987; Ghil and Mo 1991) in boreal winter, and significant EISO signals with periods of approximately 39, 19, and 16 days were found in the regional spectrum analysis of Dickey et al. (1991). Hannachi et al. (2017) summarized the progress in recognizing the intraseasonal circulation behaviors in the extratropical atmosphere of boreal winter, and numerous previous studies emphasize the strong connection between the boreal winter EISO and tropical forcing (Lau and Phillips 1986; Frederiksen and Webster 1988; Ferranti et al. 1990; Garfinkel et al. 2014; Straus et al. 2015), which was also comprehensively summarized by Stan et al. (2017).

Recent studies have increasingly recognized the significance of boreal summer EISOs, because they have been found to broadly trigger or enhance regional extreme meteorological events. Examples include flooding over East Asia (Chan et al. 2002; Liu et al. 2014, 2020; Wang 2020), South Asia (Ding and Wang 2007; Dugam et al. 2009), the Tibetan Plateau (Fujinami and Yasunari 2004; Yang et al. 2017), and the Mediterranean (Sanchez-Gomez et al. 2008) and heatwaves over North America (Teng et al. 2013), East Asia (Gao et al. 2018; Qi et al. 2019), and North Africa (Chauvin et al. 2010). Particularly, the concurrent regional extreme events over Eurasia have been found to be closely aligned with significant extratropical intraseasonal traveling waves (Kornhuber et al. 2020; White et al. 2022). Eurasian intraseasonal waves mostly feature zonal propagation along the jet waveguide but have diverse properties with different periodicities and propagating directions over different locations. Examples include midlatitude eastward-propagating waves along the subtropical westerly jet (SJ) across the Mediterranean Sea–Black Sea toward Southeast Asia (e.g., Fujinami and Yasunari 2004; Yang et al. 2014, 2017), high-latitude eastward-propagating waves along the polar front jet (PJ) across the Ural Mountains toward East Asia (Xu et al. 2020; Zhu and Yang 2021; Tang et al. 2022), and high-latitude westward-migrating waves along the PJ across Europe toward the North Atlantic (Sanchez-Gomez et al. 2008; Yang et al. 2013, 2022).

The diverse boreal summer Eurasian extratropical intraseasonal waves in previous studies mainly result from three types of perspectives. The first is using the small regional-based statistical methods like the lead–lag correlation/regression or composite analysis based on intraseasonal cases over some specific regions (Fujinami and Yasunari 2004; Liu et al. 2014; Yang et al. 2014, 2017; Cheng et al. 2021; Li et al. 2021; Zhu and Yang 2021; Gao et al. 2022; Zhong et al. 2022; Zhou et al. 2023; and many others). These studies reported the striking extratropical intraseasonal waves associated with the regional intraseasonal events but tended to statistically amplify the signals in the study target regions. The second is using the

domain-based statistical methods like the empirical orthogonal function, singular value decomposition, or singular spectral analysis over the whole mid- to high-latitude Eurasia (e.g., Yang 2001; Ding and Wang 2007; Yang et al. 2013; Sun et al. 2018; Stan and Krishnamurthy 2019). These studies did not consider the distinct components of climatological background within one domain, e.g., the subtropical and polar front jets are not intentionally separated even though they are two distinctive waveguides when the domains were selected for some conventional statistical analysis. As a result, these studies more easily captured the intraseasonal waves in the higher latitudes rather than the lower latitudes of the selected domains, although some midlatitude signals were included (Figs. S1a,b in the online supplemental material), because the atmospheric intraseasonal variability is usually larger in higher-latitude regions (Li 1990; Xu et al. 2020, also can be seen in Fig. S1c). The third is identifying the intraseasonal evolution of some mid- to high-latitude waves, which are originally reported as typical quasi-stationary teleconnections in the interannual time scale, like the Silk Road pattern in Lu et al. (2002) and Sato and Takahashi (2003), circumglobal teleconnection in Ding and Wang (2005) and Schubert et al. (2011), and British–Baikal Corridor pattern in Xu et al. (2019, 2020). These studies provided the quasi-stationary characteristics of interannual-like wave patterns in the intraseasonal time scale but ignored the potential traveling properties of the intraseasonal waves themselves. More importantly, all the above results cannot be directly applied for real-time monitoring, model evaluation, and subseasonal prediction. Therefore, similar to tropical ISO, it is necessary to objectively sort out the real dominant EISOs based on a practical method that overcomes the disadvantages of previous studies, which can be applied for operational application.

Two recent research projects further motivate the study of boreal summer EISOs. The first is the World Weather Research Programme (WWRP) and the World Climate Research Programme (WCRP) Subseasonal to Seasonal Prediction Project (S2S), launched in November 2013, with the primary goals of improving prediction skills and understanding the dynamics and climate drivers on the S2S time scale. Along with this project, several studies have reported that regional subseasonal prediction biases are ascribed to the failure of predicting extratropical intraseasonal waves, including the prediction of the heatwave in 2003 in eastern China (Qi and Yang 2019), the record-breaking mei-yu in 2020 (Yan et al. 2021b), and the onset of the South China Sea summer monsoon (Yan et al. 2021a). The second is the Transregional Collaborative Research Center "Waves to Weather" (W2W), established in July 2015, in which one of the important subtopics is to explore the role of Rossby waves in seamless prediction (10–30 days) of extremes. A recent review article about W2W has concluded that the intraseasonal Rossby waves within the jet stream may play a role in enhancing the S2S predictability of extreme events over the midlatitude regions (White et al. 2022). In addition to the two research projects mentioned above, our recent work (Yang et al. 2023, manuscript submitted to *npj Climate Atmos. Sci.*) also found that the subseasonal prediction of both 2-m temperature and atmospheric circulation over East Asia significantly exhibits

higher skill when the climate background has stronger EISO signals along the jet stream (Fig. S2; similar to Fig. 2 of Yang et al. 2023, manuscript submitted to *npj Climate Atmos. Sci.*). Therefore, a well-portrayed real-time EISO metric is urgently needed in the S2S community for better real-time monitoring, model evaluation, and subseasonal prediction.

To fill the gap of EISO study and meet the urgent need for application, the present study is first to objectively sort out and comprehensively clarify the leading intraseasonal waves along the jet streams that capture the fundamental characteristics of the mid- to high-latitude ISO signals over the Eurasian sector during boreal summer. On this basis, this study will construct real-time metrics potentially for operational real-time monitoring, subseasonal prediction, and model evaluation (Robertson et al. 2015). This study will stimulate an extratropical focus in the S2S community as a complementary component in addition to monitoring the MJO's teleconnection to the mid- to high latitudes (Vitart et al. 2017).

2. Datasets and methods

a. Meteorological datasets

Daily atmospheric fields, including geopotential height (GHT), temperature (*T*), winds [zonal (*U*) and meridional (*V*)], and potential vorticity (PV) at different levels, and 2-m air temperature (*T*$_{2m}$), are retrieved from ERA-Interim (Dee et al. 2011), with a horizontal resolution of $1.5° \times 1.5°$ and covering the period 1982–2018. The daily averaged interpolated outgoing longwave radiation (OLR) is used, which is retrieved from National Oceanic and Atmospheric Administration (NOAA), with a $2.5° \times 2.5°$ horizontal resolution. The daily Arctic Oscillation (AO) index and North Atlantic Oscillation (NAO) index are from NOAA's Climate Prediction Center. The selected period is fitted to the atmospheric fields.

b. Methods

1) STATISTICAL TOOLS

This study uses two filtering methods—the Butterworth bandpass filtering method and the real-time running-mean method—to process the daily data to isolate the specific intraseasonal components. Three steps are used for the Butterworth bandpass filter: (i) the slow climatological annual cycle is removed by subtracting the climatological mean and the first three harmonics; (ii) the synoptic fluctuations are removed by taking a 5-day running mean, and we define the processed data here as the intraseasonal signals (e.g., intraseasonal V200); and (iii) the specific intraseasonal components are obtained by the Butterworth bandpass filter (e.g., 8–25-day V200; 10–30-day V250; 10–40-day GHT250). This method has been widely used in observational work (e.g., Wang et al. 2013; Yang and Li 2016). For the real-time running-mean method, three steps are also used: (i) remove the slow climatological annual cycle by subtracting the climatological mean and the first three harmonics from the raw data; (ii) remove the lower-frequency variability by subtracting the previous N1-day running mean, as done in Wheeler and Hendon (2004) and Lee

et al. (2013); and (iii) remove the higher-frequency noise by making the previous N2-day running mean. We denote the processed data with an asterisk—for example, 8–25-day V200*, 10–30-day V250*, and 10–40-day GHT250*. Therefore, the signals extracted by this method contain no "future" information and can be applied to real-time monitoring. The rationality of this real-time running-mean method has been widely verified in many previous works (e.g., Hsu et al. 2015; Zhu and Li 2018; Wu et al. 2022). After numerous sensitivity analyses using intervals with various numbers of days for smoothing in the second and third steps, we eventually set N1 (N2) equal to 9 (3) as the best parameter to retain the 8–25-day signals, 11 (3) to retain the 10–30-day signals, and 15 (3) to retain the 10–40-day signals. A detailed comparison of the results between the two filtering methods is given in section 4.

Empirical orthogonal function (EOF) analysis is performed for the boreal summer (1 May–31 August) intraseasonal variables to extract the dominant EISO modes, with reference to the separability criterion of North et al. (1982). Normalized fields feed the EOF analysis, as in previous studies (Lee et al. 2013; Lin 2013). A power spectrum analysis is applied to analyze the periodicity and the dominant time scales of the corresponding principal components (PCs). The statistical significances of the power spectra are tested according to the method developed by Gilman et al. (1963).

Lead–lag correlation analysis and composite analysis are also applied, to identify the spatiotemporal evolutions and three-dimensional features of EISOs; and considering the strong autocorrelation of the filtered data, the number of degrees of effective freedom is calculated to determine the statistical significance, according to the method of Zwiers and Storch (1995).

2) ENERGY ANALYSIS

To explore the energy conversion of the core region and possible mechanisms for the growth of the EISOs, the barotropic and baroclinic energy conversion (CK and CP) are considered in this study. According to Hoskins et al. (1983), Maloney and Hartmann (2001), and Du and Lu (2021), the CK and CP can be calculated as follows:

$$\text{CK} = \frac{v'^2 - u'^2}{2}\left(\frac{\partial \overline{u}}{\partial x} - \frac{\partial \overline{v}}{\partial y}\right) - u'v'\left(\frac{\partial \overline{u}}{\partial y} + \frac{\partial \overline{v}}{\partial x}\right),$$

$$\text{CP} = -\frac{f}{S}\left(v'T'\frac{\partial \overline{u}}{\partial p} - u'T'\frac{\partial \overline{v}}{\partial p}\right),$$

where *f* is the Coriolis parameter; *p* is the pressure; and *S* is the static stability, which is defined as $(R\overline{T}/C_p p) - (\partial \overline{T}/\partial p)$, in which C_p is the specific heat and *R* is the gas constant of dry air. An overbar denotes the summer mean state, and a prime is the intraseasonal perturbation. A positive value of CK and CP represents energy conversion from the mean flow to the intraseasonal perturbation by barotropic and baroclinic processes, respectively (Kosaka and Nakamura 2006, 2010).

TABLE 1. Definitions of eight phases based on the normalized PC1 and PC2 for strong events: $(PC1^2 + PC2^2)^{1/2} > 1.5$.

Phase	Definition
1	PC1 < 0 and PC2 > 0 and abs(PC1) < abs(PC2)
2	PC1 < 0 and PC2 > 0 and abs(PC1) > abs(PC2)
3	PC1 < 0 and PC2 < 0 and abs(PC1) > abs(PC2)
4	PC1 < 0 and PC2 < 0 and abs(PC1) < abs(PC2)
5	PC1 > 0 and PC2 < 0 and abs(PC1) < abs(PC2)
6	PC1 > 0 and PC2 < 0 and abs(PC1) > abs(PC2)
7	PC1 > 0 and PC2 > 0 and abs(PC1) > abs(PC2)
8	PC1 > 0 and PC2 > 0 and abs(PC1) < abs(PC2)

The efficiencies of the energy conversions are also evaluated, by the metric of replenishing time scales (τ), and the τ_{CK}, τ_{CP}, and τ_{CK+CP} can be calculated as

$$\tau_{CK} = \frac{\{KE\}}{\{CK\}},$$

$$\tau_{CP} = \frac{\{APE\}}{\{CP\}},$$

$$\tau_{CK+CP} = \frac{\{KE + APE\}}{\{CK + CP\}},$$

where KE is the intraseasonal perturbed kinetic energy and APE is the intraseasonal available potential energy. The curly braces {} denote the spatial and vertical integration from 1000 to 100 hPa. The KE and APE are calculated as

$$KE = \frac{(u'^2 + v'^2)}{2},$$

$$APE = \frac{RT'^2}{2S}.$$

according to Kosaka and Nakamura (2006), Huang et al. (2020), and Du and Lu (2021), a positive τ represents a net energy gain of the intraseasonal perturbation, and a shorter τ can be regarded as being more effective.

3) DEFINITIONS FOR EISOS' PHASE SPACE, HEATWAVES, AND BLOCKINGS

Similar to the tropical ISO indices of Wheeler and Hendon (2004), Kikuchi et al. (2012), and Lee et al. (2013), a two-dimensional phase space defined by the first two normalized PCs is constructed. It is convenient to identify the state and location of the EISOs using a point in the diagram. We define eight phases to track the spatiotemporal evolution of the strong events in Table 1.

To examine the impact of the retrieved EISO waves on the extreme heating events, a relative threshold is used to choose the heatwave events over the specific regions. Following the approach of Liu et al. (2008) and Chen and Zhai (2017), a heatwave event is defined as three or more successive days of regional-averaged T_{2m} exceeding the 90th percentile of the climatology, which is the 31-day window centered on each calendar day during 1982–2018. Also, the day on which the

maximum T_{2m} occurs is used to represent the particular heatwave event.

The linkages between the EISOs and blocking events are also examined, as follows. According to the methods of Lejenäs and Økland (1983) and Tibaldi and Molteni (1990), the southern 500 hPa GHT (GHT500) gradient (GHGS) and the northern GHT500 gradient (GHGN) are first computed at each longitude as

$$GHGS = \left[\frac{GHT(\varnothing_o) - GHT(\varnothing_s)}{\varnothing_o - \varnothing_s}\right],$$

$$GHGN = \left[\frac{GHT(\varnothing_n) - GHT(\varnothing_o)}{\varnothing_n - \varnothing_o}\right],$$

where $\varnothing_n = 80°N + \delta$, $\varnothing_o = 60°N + \delta$, $\varnothing_s = 40°N + \delta$, $\delta = -5°, 0°, 5°$. A given longitude on a given day is defined as blocked if there is at least one value of δ that satisfies both of the following criteria: (i) GHGS > 0 m degree^{-1}; (ii) GHGN < −10 m degree^{-1}. Note that a 5-day running mean is applied to the GHT500 prior to calculating both GHGS and GHGN to extract potential blocking events of sufficient duration. In this study, a Ural Mountains blocking (UB)/Lake Baikal blocking (LB) event is defined when at least one longitude between 30° and 60°E/90° and 120°E is blocked; and according to this definition, 993 UB and 476 LB events are selected in boreal summer from 1982 to 2018.

3. One SJ-related EISO and two PJ-related EISOs over Eurasia

a. SJ- and PJ-related domains over Eurasia

As many previous studies have shown, EISOs over Eurasia feature zonally traveling waves trapped mostly along the jet streams (Branstator 2002; Martius et al. 2010; Giannakaki and Martius 2016; Wirth et al. 2018). Two types of jet streams over Eurasia, respectively named SJ and PJ, have been known in previous knowledge (Yang and Zhang 2008; Lu et al. 2013 for SJ; Panetta 1993; Lee 1997; Huang et al. 2014 for PJ). To overcome the disadvantages in the previous studies pointed out in section 1, this study intentionally separates the Eurasian continent into two regions, respectively, including two distinct jet streams. Figure 1a shows the Eurasian zonally averaged (15°W–150°E) climatological U wind at different pressure levels in boreal summer, and the core region of the climatological SJ and PJ with the maximum zonal wind speed is respectively located nearly at 200 and 250 hPa, which is consistent with to previous studies. Figure 1b displays the 200 hPa climatological U wind (U200), and the maximum jet core concentrates between the latitudes of 25° and 55°N and the longitudes of 15°W and 150°E, which represents the location of SJ. According to Iwao and Takahashi (2008) and Xu et al. (2019), PJ stream is better identified by the 250 hPa PV meridional gradient rather than U wind. Hence, we recognize the domain (55°–85°N, 25°–150°E) as the PJ's location over the Eurasian continent according to the climatological spatial distribution of the 250 hPa PV meridional gradient in boreal summer displayed in Fig. 1c.
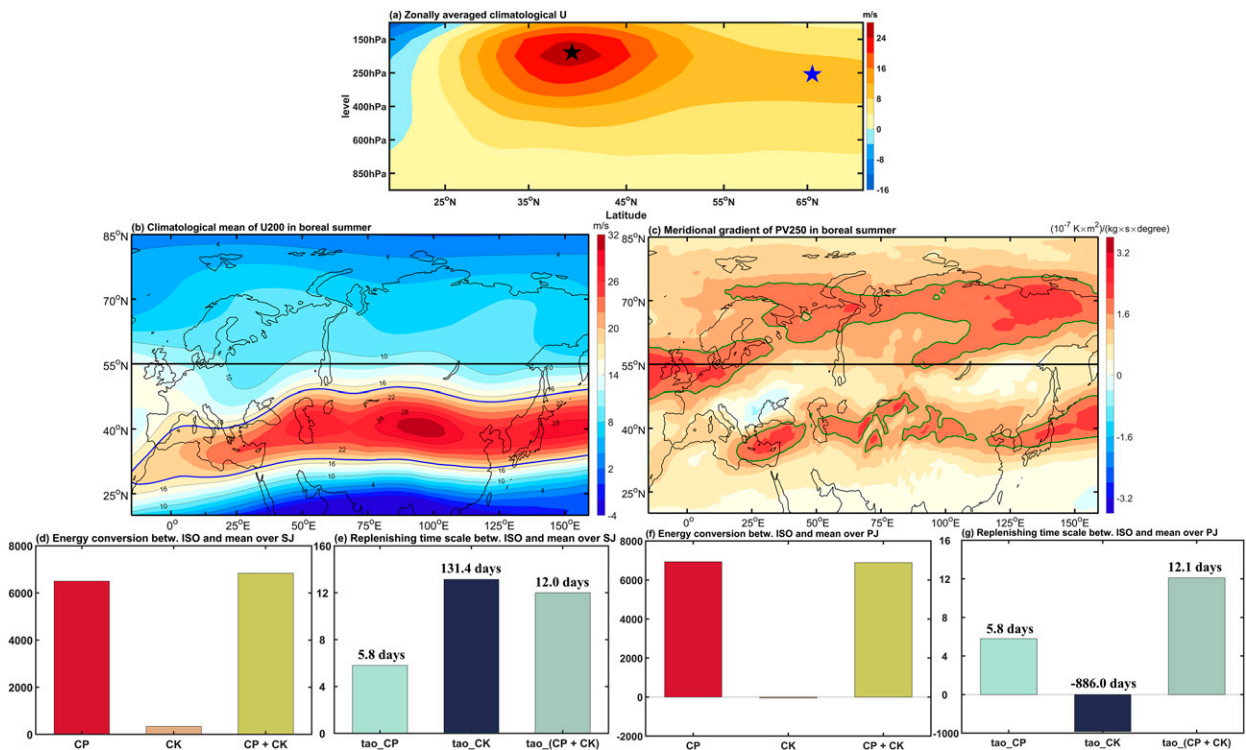
FIG. 1. (a) Zonally averaged (15°W–150°E) climatological U wind (shading; unit: m s^{-1}) at different pressure levels over the Eurasian continent in boreal summer. The black and blue stars roughly denote the altitude of SJ and PJ, respectively. (b) Climatological U200 (shading; unit: m s^{-1}) in boreal summer. The blue line is the boreal summer–averaged U200 contour of 18 m s^{-1}, which roughly denotes the SJ's location. (c) The meridional gradient of the climatological PV250 (shading; unit: 10^{-7} K m^2 kg^{-1} s^{-1} degree^{-1}) in boreal summer. The green line is the meridional gradient of PV250 contour of 1.6×10^{-7} K m kg^{-1} s^{-1} degree^{-1}, which roughly denotes the location of the PJ. (d) Total energy conversion (unit: m^4 s^{-3} hPa) integrated from 1000 to 100 hPa over the Eurasian SJ region between the ISO perturbation and mean flow in boreal summer. (e) The replenished time scales (tao; unit: day) over the Eurasian SJ region. (f),(g) As in (d) and (e), but for PJ region.

In terms of the selected SJ and PJ regions over the Eurasian continent, we calculate the energy conversions and conversion efficiencies between the intraseasonal component and mean state in boreal summer, as shown in Figs. 1d–g. As a result, both SJ and PJ regions are the sink of intraseasonal energy in boreal summer, in which the baroclinic energy conversions are dominant. The energy analysis above shows that the energy prefers the conversion from the mean state to intraseasonal eddy in boreal summer over the SJ and PJ region (dominantly through baroclinic processes) and facilitates the developments of intraseasonal disturbances, which further illustrates that both SJ and PJ potentially feature the active intraseasonal signals.

b. SJ-related eastward-propagating EISO mode

To obtain the leading EISO mode trapped in SJ, a conventional EOF analysis is carried out for the intraseasonal 200 hPa *V* wind (V200) over the SJ region. Here V200 is selected as the optimal variable to best describe EISOs because of its superiority in identifying Rossby waves (Lu et al. 2002; Hu et al. 2018; Wirth et al. 2018). First, as shown in Fig. 2a, EOF1 and EOF2, which can explain 13.4% and 12.7% variances, respectively, are not separable but distinguishable from the rest of the modes, according to the criterion proposed by North et al.

(1982). Figures 2b and 2c depict the spatial distributions of the intraseasonal V200 for the leading two EOF modes. As can be seen, EOF1 and EOF2 show a similar pattern of zonal wavenumber 3 along the SJ over the Eurasian continent, but with a quadrature phase relationship. Meanwhile, the spectrum analysis of PC1 and PC2 reveals that the dominant temporal periodicities of the first two EOFs share 8–25 days with a peak periodicity of about 18 days, which can explain 46.7% and 51.8% of the variance of the original PC1 and PC2, respectively (Figs. 2d,e). Also, the temporal correlation coefficient between them is nearly 0.30 (−0.36), exceeding the 95% significance level, when PC1 leads (lags) PC2 by 3–4 days, which corresponds to approximately a quarter of their life cycle (Fig. 2f). The similar static spatial structures of EOF1 and EOF2 and the temporal characteristics of the corresponding PCs indicate that the wave patterns of EOF1 and EOF2 may be two different phases of the same wave train.

To further determine the consistency of the leading two modes from a physical point of view, the temporal–zonal Hovmöller diagrams of the SJ-meridionally averaged lead–lag correlation coefficient between the 8–25-day V200 and 8–25-day PCs are calculated. They share the similar eastward propagations with the phase velocity speed of 3.1 m s^{-1} and group
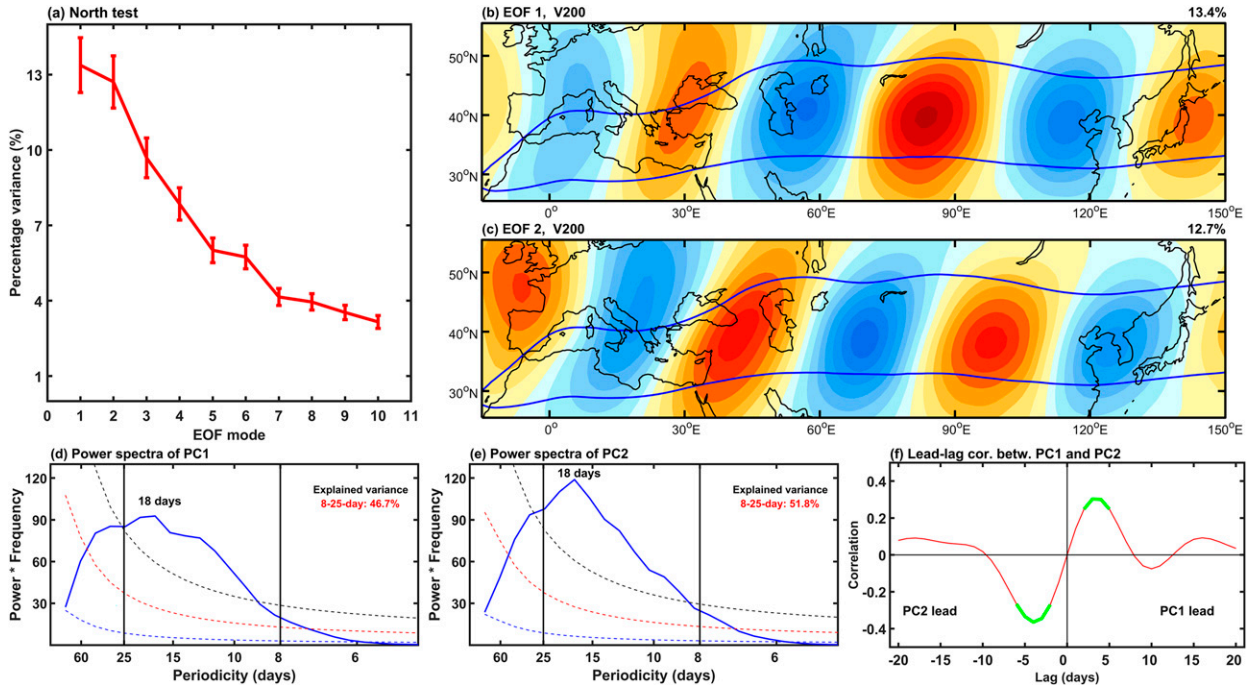
FIG. 2. (a) Percentage variance (unit: %) explained by the first 10 EOF modes for the boreal summer intraseasonal V200 over the Eurasian SJ region. The bars represent one standard deviation of the sampling errors. Spatial distributions of the (b) first and (c) second EOF modes of the boreal summer intraseasonal V200 over the Eurasian SJ region. The blue line is the boreal summer–averaged U200 contour of 18 m s^{-1}, which denotes the SJ's location. The power spectra of the corresponding (d) PC1 and (e) PC2. The red dashed line denotes the Markov red noise spectrum, and the blue and green dashed lines represent the a priori and a posteriori 99% confidence, respectively. (f) The temporal lead–lag correlation between the first two PCs, in which the green part of the line exceeds the 95% confidence level.

velocity speed of 23.6 m s^{-1} (Figs. S3a,b), and consistent vertical quasi-barotropic structure with the maximum amplitudes of 150–200 hPa (Figs. S3c,d). Meanwhile, the spatial lead–lag correlation coefficient also confirms the significant relationship of the first two EOFs, in which the spatial correlation coefficient reaches 0.91 (−0.93), far exceeding the 99% significance level, when EOF1 leads (lags) EOF2 by 4 days (Fig. S3e). In addition to similar spatiotemporal evolutions and characteristics, the energy conversions associated with EOF1 and EOF2 are almost similar, in which both EOFs harvest energy from background flow through baroclinic processes throughout their lifetime (Fig. S3f). Therefore, the first two EOFs have been confirmed to be a pair and together represent an 8–25-day eastward-propagating wave along the SJ. Like the tropical ISOs represented by the MJO and BSISO indices, a two-dimensional metric for retrieving the EISO wave trapped over the SJ, named EISO-SJE, is constructed using a combination of the 8–25-day PC components from the EOF1 and EOF2 of V200 over the SJ region.

To clarify the spatiotemporal characteristics of EISO-SJE, we select strong events based on the eight-phase diagram of the EISO-SJE metric (Table 1), and construct the composite 8–25-day V200 in each phase (Fig. 3). Similar to the MJO and BSISO indices, the strong events are defined in this study by the amplitude being greater than 1.5 [i.e., (PC1^2 + PC2^2)$^{1/2}$ > 1.5]. Additionally, we also examined other smaller amplitudes, such as greater than 0.8 or 1, as the criteria for strong events, and

find that the composite EISO-SJE is similar but with a slightly weaker amplitude. The EISO-SJE has a zonal wavelength of about 4400 km between 25° and 55°N. This eastward-propagating EISO-SJE initiates over the Northeast Atlantic to the west of Great Britain, at the exit of the North America–North Atlantic jet core. When the initial perturbation lands on the Eurasian continent, it is trapped by the Eurasian continental SJ and the meridional perturbation amplifies. Afterward, EISO-SJE moves eastward with a phase speed of about 3.1 m s^{-1} along the SJ over the Eurasian continent, amplifies over the Black Sea–Caspian Sea–arid central Asia area (the Iranian–Tibetan Plateau regions), and weakens near coastal East Asia. The spatial features of EISO-SJE are also examined in the middle and lower troposphere, revealing that the abovementioned horizontal structures and eastward propagation can be clearly seen in the mid-to-lower troposphere, but with relatively weaker amplitude (not shown). The composite EISO-SJE has similar wave characteristics to EOF1 and EOF2 individually, further illustrating that the constructed EISO-SJE metric is reasonable. The EISO-SJE-like intraseasonal wave does have been exhibited in some regional-based studies (e.g., Fujinami and Yasunari 2004; Yang et al. 2014, 2017), but the amplitude over some specific regions is statistically amplified due to the limitation of one-point statistical methods as mentioned in section 1.
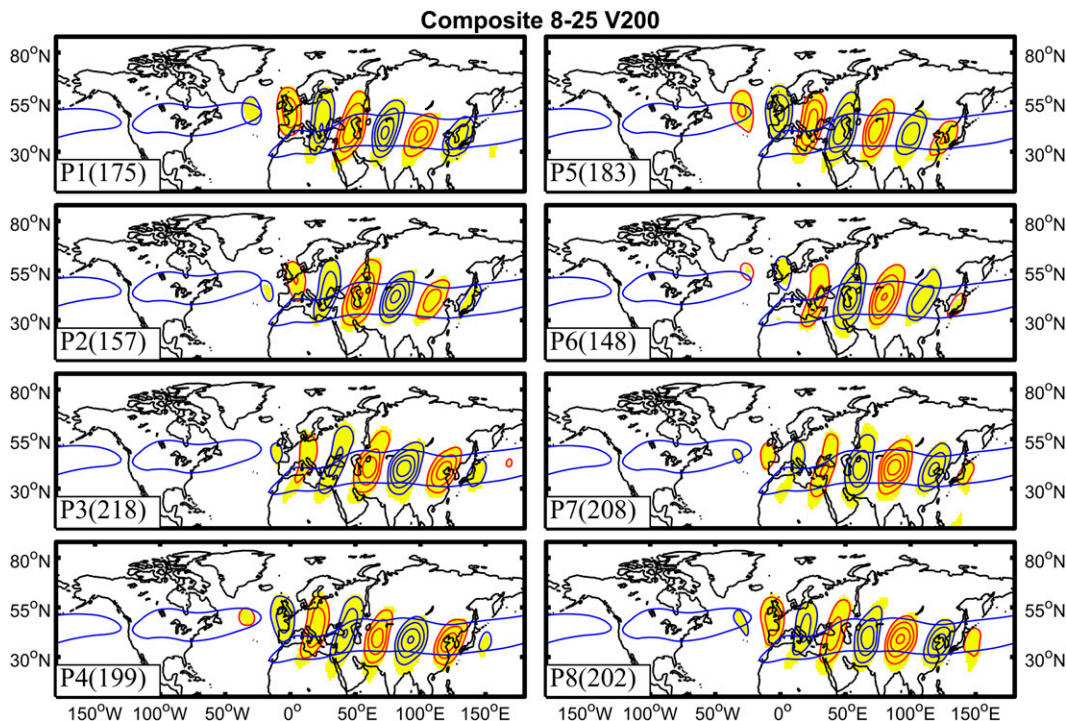
Composite 8-25 V200

FIG. 3. Composite 8–25-day V200 (contours; unit: m s^{-1}; interval: 1.5 m s^{-1}; shading: above the 95% confidence level) for eight phases based on EISO-SJE strong events. The blue line is the boreal summer–averaged U200 contour of 18 m s^{-1}, which denotes the SJ's location. The red (blue) contours are the positive (negative) values.

c. PJ-related eastward-propagating EISO mode

PJ is the high-latitude dominant waveguide facilitating the zonal propagation of the Rossby wave (Branstator 2002; Wirth et al. 2018; White et al. 2022) over the Eurasian continent. We perform an EOF analysis for the intraseasonal 250 hPa *V* wind (V250) over the PJ region. As shown in Fig. 4a, EOF1 and EOF2 are a pair and significantly separable from the rest of the modes. Together, they explain 41.0% of the variance of the intraseasonal variation. The spatial patterns of the first two EOFs are shown in Figs. 4b and 4c. And both have zonal wavenumber 1.5 over the PJ region, but with a quadrature phase relationship with each other. The spectrum analysis applied to the PC1 and PC2 shows the first two PCs together have a dominant periodicity of 10–30 days and share the same peak periodicity of 20 days (Figs. 4d,e). And their corresponding 10–30-day components can explain 48.3% and 53.4% variance of the raw PC1 and PC2, respectively. In addition, the temporal lead–lag correlation of EOF1 and EOF2 also shows their significant coherence (Fig. 4f), in which the temporal correlation coefficient of their PCs is nearly 0.24 (−0.21) when PC1 leads (lags) PC2 by 3–5 days.

The first two EOFs-related temporal–zonal Hovmöller diagrams and zonal–vertical cross sections meridionally averaged over PJ are examined. The results show that EOF1 and EOF2 share a similar propagating phase speed of 3.8 m s^{-1} and group velocity of 25.8 m s^{-1} (Figs. S4a,b). Moreover, EOF1 and EOF2 also have a similar vertical structure, which features a quasi-barotropic structure (Figs. S4c,d). Meanwhile,

the spatial lead–lag correlation of EOF1 and EOF2 also shows their coherence (Fig. S4e). The spatial correlation coefficient reaches 0.84 (−0.83) when EOF1 leads (lags) EOF2 by 4 days. Their related energy conversions are also examined, as shown in Fig. S4f. As can be seen, EOF1 and EOF2 feature similar energy conversions, in which baroclinic processes exert a vital positive contribution in the whole life cycle of both EOF1 and EOF2, while barotropic processes play a negligible role. Since EOF1 and EOF2 obtained over the PJ region have similar three-dimensional spatial structures, dominant periodicity, spatiotemporal evolutions, and energy conversion processes, they have been verified to be two different phases of the same wave train and together represent a 10–30-day eastward-propagating wave along the PJ. Therefore, a two-dimensional metric for retrieving the eastward-propagating EISO along the PJ, named EISO-PJE, is constructed using the combination of the 10–30-day PC components from EOF1 and EOF2 of V250 over the PJ region.

Similar to EISO-SJE, we can better portray EISO-PJE by compositing the spatial distributions of the 10–30-day V250 in eight phases of the EISO-PJE metric (Fig. 5). EISO-PJE is characterized by a zonal wavelength of about 4200 km along the latitudes of 55°–85°N, and a phase speed of about 3.8 m s^{-1}. It features eastward migration with zonal wavenumber 2 spanning over the high-latitude Eurasian continent. EISO-PJE originates near Scandinavia, where the bifurcation of the North America–North Atlantic jet and the PJ is situated; enhances over the East European Plain;
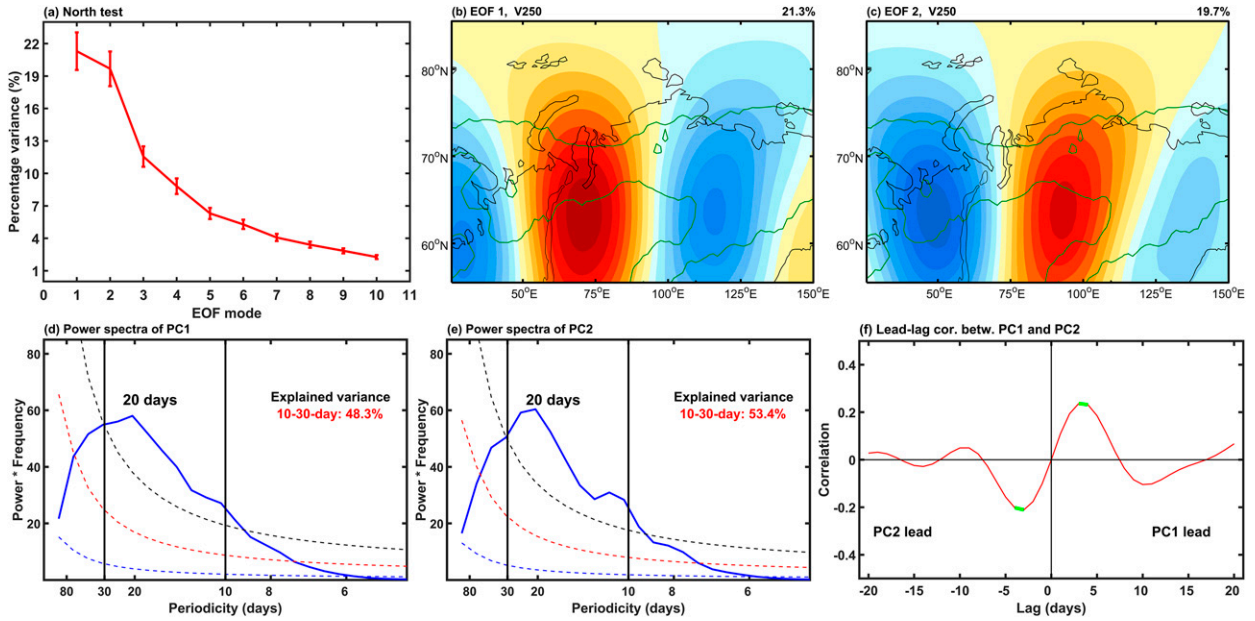
FIG. 4. As in Fig. 2, but for the intraseasonal V250 over the Eurasian PJ region.

crosses the Ural Mountains and the West Siberian Plain; and decays over the Okhotsk region.

Note that though both EISO-SJE and EISO-PJE exhibit eastward propagation, the different features between them can be clearly identified. First, they propagate along the different

waveguides, which implies they may have distinct dynamic processes. Second, the peak periodicity of EISO-PJE is about 20 days, which is longer than the 18 days of EISO-SJE. Third, the maximum amplitudes of EISO-PJE are located at 250–300 hPa, which is lower than that of EISO-SJE at 150–200 hPa. Furthermore, the
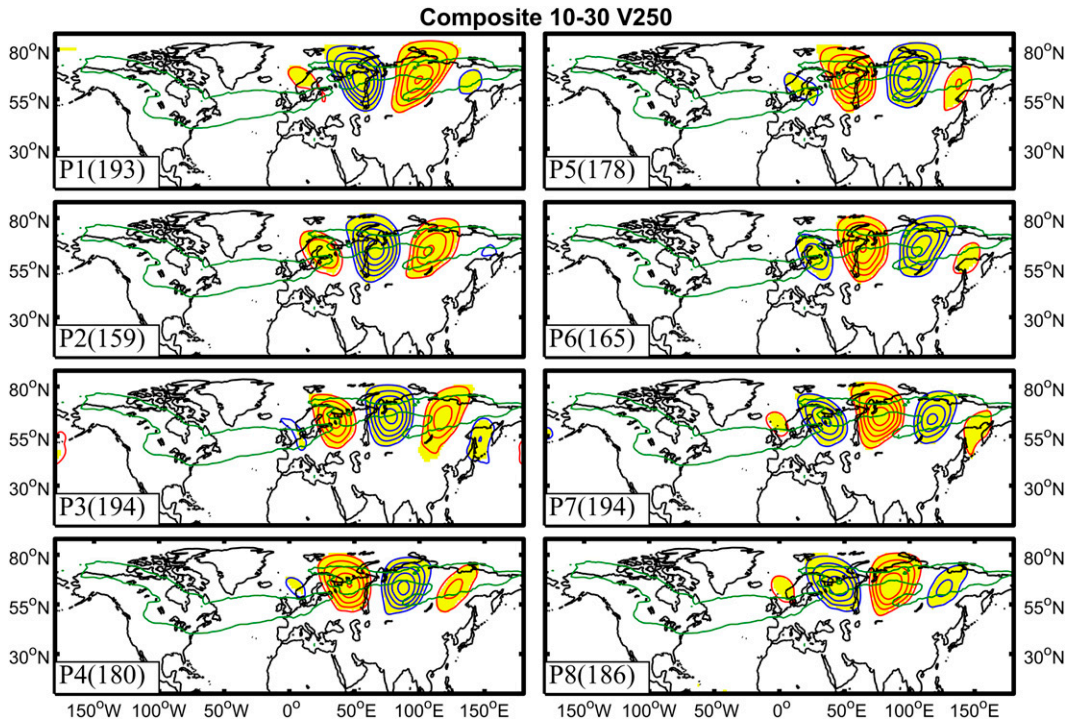
FIG. 5. As in Fig. 3, but for the composite 10–30-day V250 for eight phases based on EISO-PJE strong events (contours; unit: m s^{-1}; interval: 1.5 m s^{-1}; shading: above the 95% confidence level). The green line is the meridional gradient of PV250 contour of 1.6×10^{-7} K m kg^{-1} s^{-1} degree^{-1}, which roughly denotes the location of the PJ.
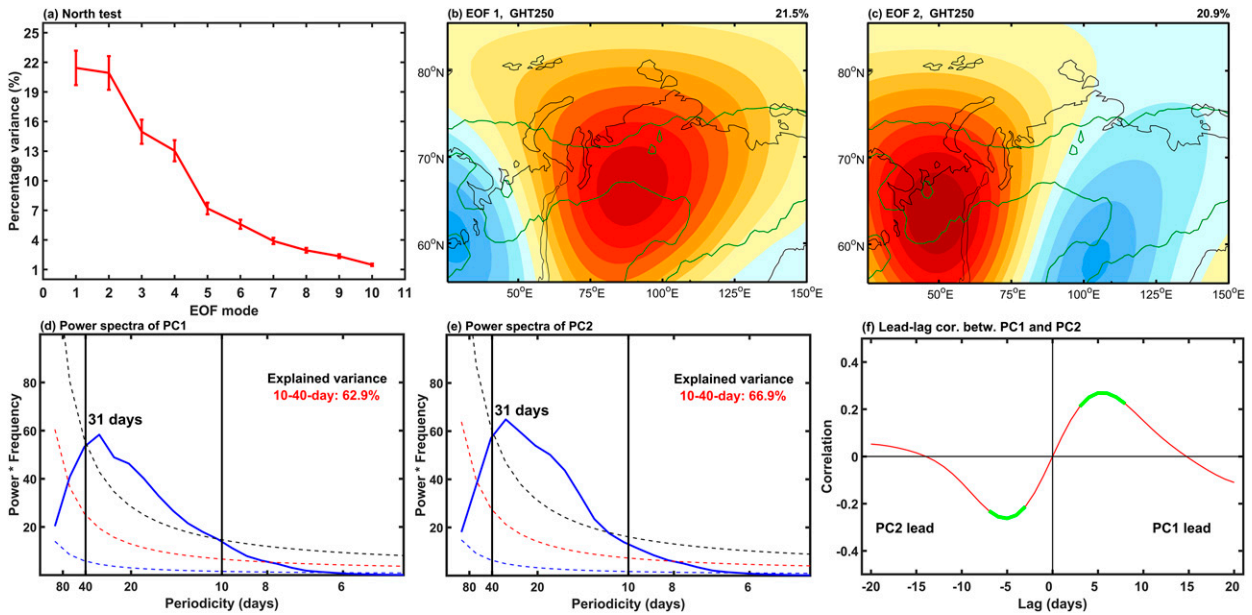
FIG. 6. As in Fig. 2, but for the intraseasonal GHT250 over the Eurasian PJ region.

historical cases, which will be displayed in section 4a, demonstrate their independent occurrences. For example, a single EISO-PJE occurred during 12–25 June 1982, a single EISO-SJE appeared during 12–23 July 2017, and EISO-PJE and EISO-SJE simultaneously appeared during 5–23 July 1989.

d. PJ-related westward-propagating EISO mode

As mentioned in the introduction, there also exists a westward-propagating EISO over the Eurasian continent along the PJ in boreal summer, which has considerable effects on the Eurasian temperature variation, GHT variation near the Ural Mountains, and sea ice variation over the Barents Sea (Yang et al. 2013; Zhu and Yang 2021; Yang et al. 2022), and this westward-propagating atmospheric intraseasonal wave found in these works is through analyzing the GHT field. Therefore, in this section, we attempt to conduct the EOF analysis for the intraseasonal GHT250 over the PJ region. As shown in Fig. 6a, EOF1 and EOF2 are a pair and can be well distinguished from the rest of the modes, together explaining 42.4% of the variance. Figures 6b and 6c display the spatial patterns of EOF1 and EOF2, and they have the same spatial scale but with a quadrature relationship. The spectrum analysis of PC1 and PC2 shows that the bulk of their variance is concentrated at 10–40 days, with a peak of 31 days, and the fractional variances in the 10–40-day bands account for 62.9% and 66.9% of the original PC1 and PC2, respectively (Figs. 6d,e). The significant lead–lag correlation between EOF1 and EOF2 reveals that when EOF1 leads (lags) EOF2 by 4–6 days, the temporal correlation coefficient is 0.27 ($-$0.26), exceeding the 95% significance level (Fig. 6f).

We similarly carry out the first two EOFs-related temporal–zonal Hovmöller diagrams and zonal–vertical cross sections along PJ. It is found that EOF1 and EOF2 share a similar westward propagation, with a phase speed of 4.0 m s^{-1} (Figs. S5a,b),

and a similar quasi-barotropic structure (Figs. S5c,d). The spatial lead–lag correlations between EOF1 and EOF2 are also examined, revealing that when EOF1 leads (lags) EOF2 by 4–6 days, the spatial correlation coefficient reaches up to 0.80 ($-$0.60), which exceeds the 99% significance level (Fig. S5e). The energy analysis is also applied for the whole life cycle associated with EOF1 and EOF2, as shown in Fig. S5f. The energy conversions suggest that both EOF1 and EOF2 can obtain the ISO energy from the summer mean flow mainly via baroclinic processes. Therefore, a two-dimensional metric for retrieving the westward-propagating EISO wave, named EISO-PJW, is constructed using the combination of the 10–40-day PC components from EOF1 and EOF2 of GHT250 over the PJ region. We then composite the 10–40-day GHT250 at EISO-PJW eight phases, as shown in Fig. 7. EISO-PJW shows a wavenumber-1 structure between 65° and 85°N, with a wavelength of about 5600 km and a phase speed of about 4.0 m s^{-1}. It features westward migration from the central Siberian Plateau to Greenland, enhances near the Ural Mountains, and weakens over Scandinavia. This EISO-PJW mode covers the major features reported in previous case studies, e.g., the Ural Mountains intraseasonal westward-propagating waves in Zhu and Yang (2021) and a westward-propagating wave causing a European extreme event (Sanchez-Gomez et al. 2008).

4. Real-time metrics of boreal summer EISOs over Eurasia

One SJ-related EISO (EISO-SJE) and two PJ-related EISOs (EISO-PJE and EISO-PJW) have been well separated and comprehensively portrayed in section 3. A critical aim of identifying these three dominant EISOs is to serve real-time monitoring, subseasonal prediction, and model evaluation. Therefore, this section will first build up real-time metrics based on the
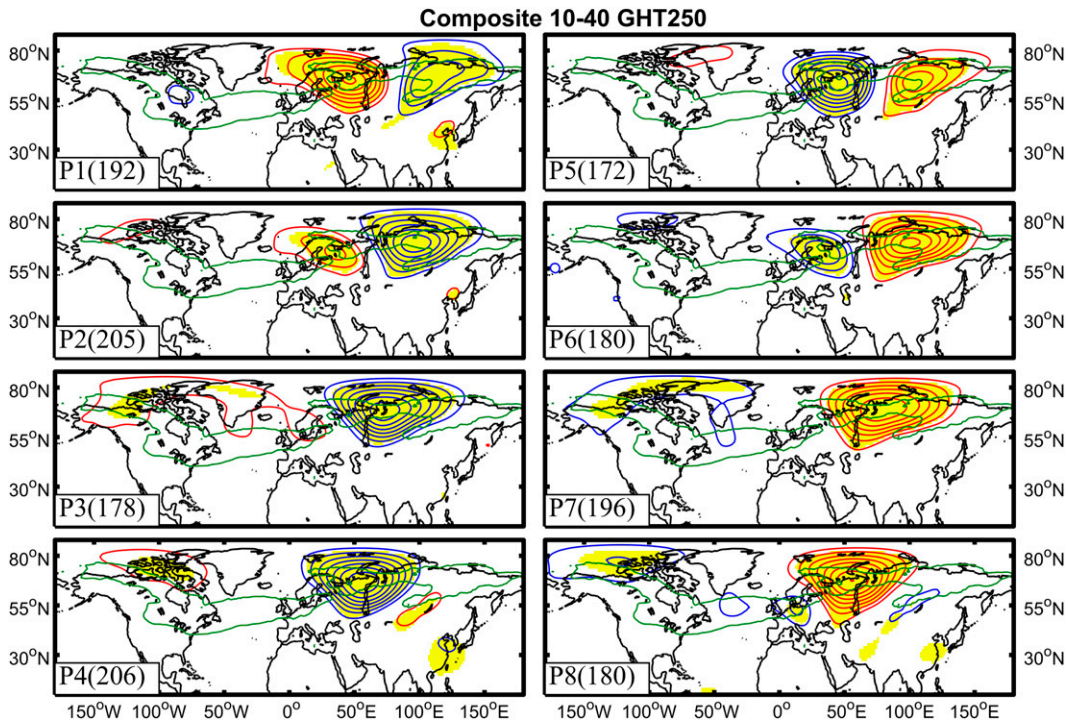
FIG. 7. As in Fig. 3, but for the composite 10–40-day GH250 for eight phases based on EISO-PJW strong events (contours; unit: gpm; interval: 10 gpm; shading: above the 95% confidence level).

dominant EISOs, verify their utility, and then explore their relations with extreme events (heat) and important extratropical synoptic systems (e.g., blocking) based on the real-time metrics.

a. Real-time metrics

To develop the real-time metrics like that of the MJO or BSISO, we use a real-time running-mean method to process the daily circulation variables (V200 for EISO-SJE, V250 for EISO-PJE, and GHT250 for EISO-PJW) that does not use any future information and can be applied to real-time monitoring (see section 2 for details). We can obtain the real-time PCs by projecting the 8–25-day V200* (10–30-day V250*/10–40-day GHT250*) onto the first two EOFs of EISO-SJE (EISO-PJE/ EISO-PJW) obtained in section 3. The boreal summer real-time and filtered EISO-SJE, EISO-PJE, and EISO-PJW metrics in three randomly selected years, as the samples are presented in Fig. 8. As can be seen, the real-time EISO metrics possess consistent variation characteristics with the filtered ones, and the temporal correlation coefficient is 0.83/0.87 for EISO-SJE (Figs. 8a,b), 0.69/0.69 for EISO-PJE (Figs. 8c,d) and 0.74/0.74 for EISO-PJW (Figs. 8e,f) in all samples (37 years × 123 days = 4551), far exceeding the 99% significance level. The EISO-SJE, EISO-PJE, and EISO-PJW waves portrayed by the real-time metrics are also examined, and they share identical temporal and spatial evolution characteristics to the conventional filtered ones (Fig. S6).

A real-time two-dimensional phase–space diagram can easily exhibit the real-time position/pattern of the traveling waves. The all-day trajectories of EISO-SJE, EISO-PJE, and

EISO-PJW in boreal summer during 1982–2018 are plotted in Figs. 8g–i. The days outside the ring represent the strong cases. For EISO-SJE, the strong cases account for 31.8% of all boreal summer days, and the cases with a duration of at least four phases (about 8–12 days) account for 52.7% among the dates outside the circle (Fig. 8g). For EISO-PJE, the strong cases account for 31.9% of all days, in which the cases with a duration of at least four phases (about 12–15 days) account for 42.1% (Fig. 8h). For EISO-PJW, there are 32.6% strong cases in all boreal summer days, in which 31.5% cases can persist at least four phases (about 18–21 days) (Fig. 8i). The frequent occurrence and long duration of EISO-SJE, EISO-PJE and EISO-PJW demonstrate the real-time EISOs' monitoring is indispensable in S2S community.

Almost all strong cases can be real-time monitored, and here, four monitoring cases are given as examples to demonstrate the utility of the real-time metrics. The first case is an evident SJ-trapped wave that propagates eastward along the SJ during 12–23 July 2017 (Fig. 9a). Accordingly, this intraseasonal wave can be accurately captured by the real-time EISO-SJE metric as shown in the two-dimensional phasespace diagram (Fig. 9b). The second case, a PJ-trapped wave propagating eastward during 12–25 June 1982, is well monitored by the real-time EISO-PJE metric shown in Figs. 9c and 9d. The third, a PJ-trapped wave traveling westward during 10–31 August 1990, is well exhibited by a real-time EISO-PJW metric (Figs. 9e,f). The last example shows a double-wave case in which the SJ-trapped and PJ-trapped waves coincide during
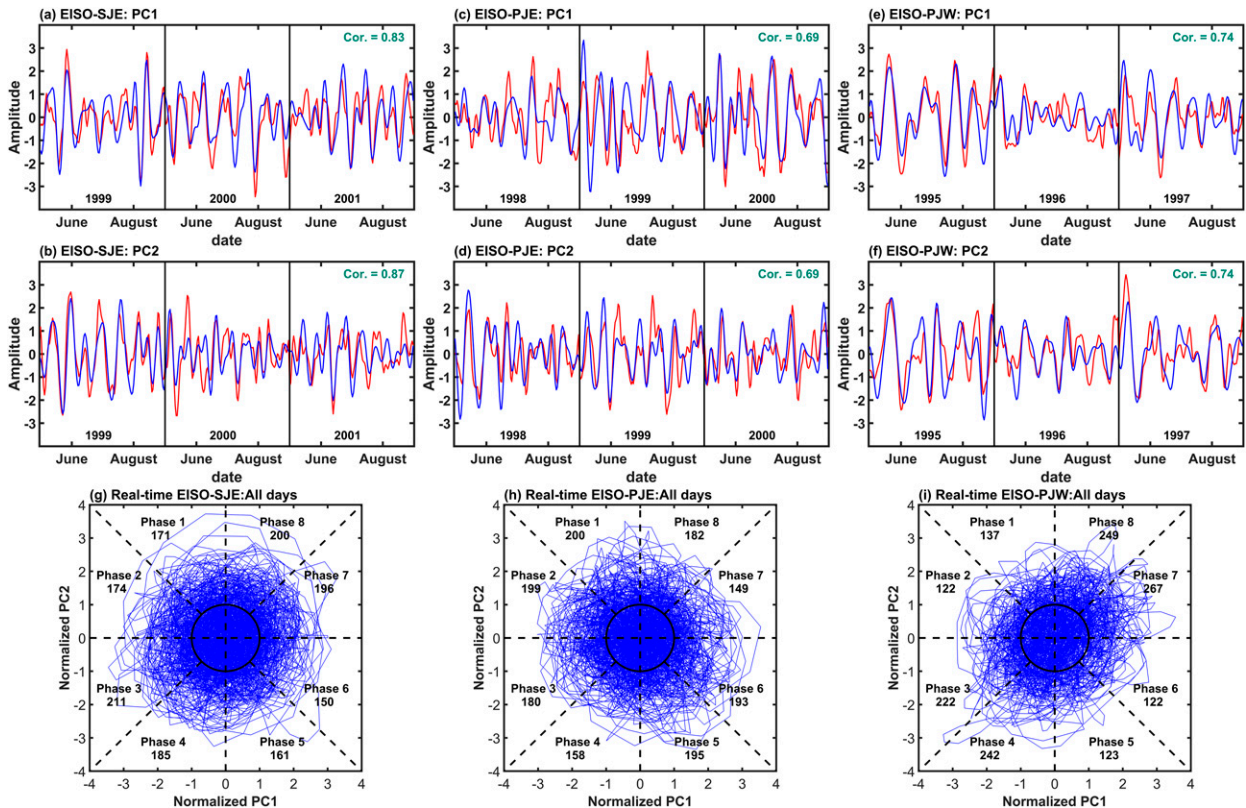
FIG. 8. Real-time (red lines) and filtered (blue lines) time series of (a) PC1 and (b) PC2 for EISO-SJE metric during boreal summer. (g) Real-time EISO-SJE phase-by-space curves for all boreal summer days from 1982 to 2018. (c),(d),(h) and (e),(f),(i) As in (a), (b), and (g), but for EISO-PJE/EISO-PJW metric.

5–23 July 1989. Correspondingly, the metrics can simultaneously capture their features, as shown in Figs. 9g and 9h.

b. Relation with the extreme events and blockings

It has been reported that the regional air temperature variability and heat extremes are evidently influenced by the atmospheric ISO (Gao et al. 2018; Kueh and Lin 2020). Figure S7 shows the composite T_{2m} anomaly overlaid with the 8–25-day (10–30-day/10–40-day) 500 hPa GHT (GHT500) based on the strong events in each phase of real-time EISO-SJE (EISO-PJE/EISO-PJW) metric. Note that the T_{2m} anomaly here is the original variable representing the unfiltered anomaly of the real surface air temperature. And the results confirm significant footprints of the three EISOs on the subseasonal variation of the real surface air temperature along their propagating tracks. The positive/negative intraseasonal GHT500 nearly coincides with the unfiltered warm/cold T_{2m} anomaly (Fig. S7). And the in-phase relationship between EISOs and temperature change indicates that the variations of the adiabatic processes associated with EISOs contribute to the surface air temperature variation on the subseasonal time scale, which is consistent with several previous local studies (Qi et al. 2019; Kueh and Lin 2020).

To further examine the impacts of the EISOs on heat extremes, four mid- to high-latitude regions are chosen (southwestern Europe and northwestern China for EISO-SJE, east of the Ural Mountains for EISO-PJE, and East European Plain for EISO-PJW; black frames in Fig. S7), which correspond to the most significant footprints of EISOs. Meanwhile, these regions are more frequently hit by summer heatwaves (e.g., Robine et al. 2008; Barriopedro et al. 2011; Tomczyk et al. 2017; Wang et al. 2017). The results exhibit that the occurrence of heatwaves is closely related to certain specific phases of EISOs (Fig. 10). For southwestern Europe, 62.1% of all 63 heatwaves appear in phases 1–3 of EISO-SJE, with phase 2 having the most, at 27.1% (Fig. 10a). For northwestern China, heatwaves appear most frequently in phases 5 and 6 of EISO-SJE (50.8%), and secondarily in phases 4 and 7 (28.8%), among 56 heatwave cases (Fig. 10b). For the east of the Ural Mountains area, 53.6% of all 56 regional heatwaves appear in phases 4 and 5 of EISO-PJE (Fig. 10c), and for the East European Plain, 58.9% of all 68 heatwave events appear in phases 8 and 1 of EISO-PJW (Fig. 10d). To further understand why the heatwave occurrences in these four regions are linked to certain specific EISOs' phases, the temperature budget equation in the lower troposphere over these four study regions was diagnosed in these preferred phases, respectively (Fig. S8). As a result, the adiabatic process plays the dominant role in warming all four target regions in these preferred phases. Accordingly, the high-pressure anomalies, respectively embedded in three EISO waves, are located over the heatwave areas
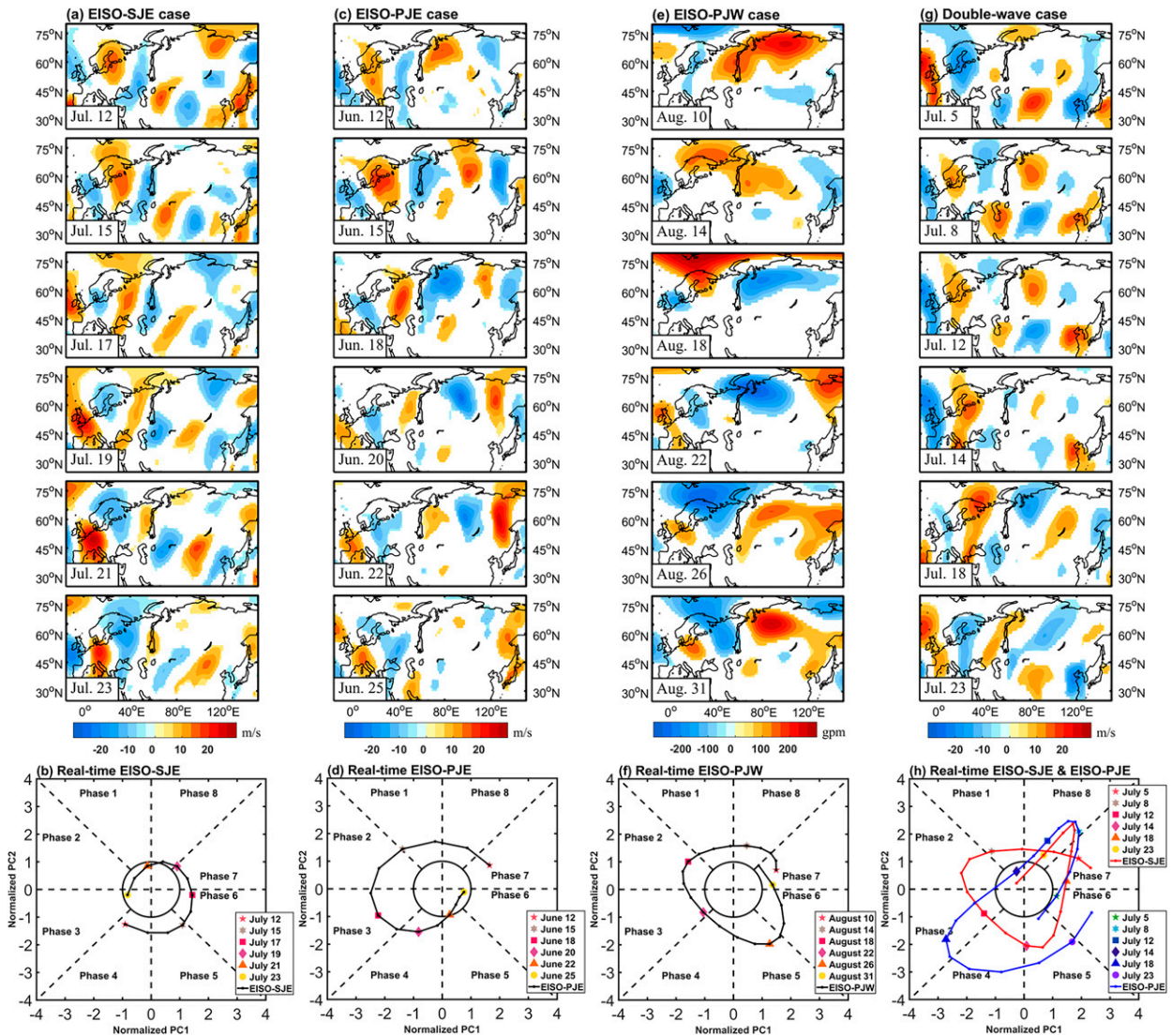
FIG. 9. Spatiotemporal evolutions of the intraseasonal (a) V200 (shading; unit: m s^{-1}) during 12–23 Jul 2017, (c) V250 (shading; unit: m s^{-1}) during 12–25 Jun 1982, (e) GHT250 (shading; unit: gpm) during 10–31 Aug 1990, and (g) V200 (shading; unit: m s^{-1}) during 5–23 Jul 1989. V200 and V250 (GHT250) greater than −5 (−50) and less than 5 (50) are ignored. Day-by-day curves for real-time (b) EISO-SJE during 12–23 Jul 2017, (d) EISO-PJE during 12–25 Jun 1982, (f) EISO-PJW during 10–31 Aug 1990, and (h) EISO-SJE and EISO-PJE during 5–23 Jul 1989.

(Fig. S7), which provides favorable conditions for the occurrence of heatwaves via increased adiabatic heating. The above-mentioned close relationship indicates that EISOs can provide potential precursory signals for subseasonal prediction over the regions along their paths.

Ural Mountains blocking (UB) and Lake Baikal blocking (LB) frequently occur over Eurasia in boreal summer (Diao et al. 2006; Tyrlis and Hoskins 2008; Liu et al. 2018; He et al. 2019), and are located along the pathways of high-latitude EISOs. Besides, they often contribute to extreme meteorological events (Kautz et al. 2022), including the hydrological extremes (Lenggenhager et al. 2019), heatwaves (Rodrigues et al. 2019), and droughts (Beniston and Diaz 2004; Schneidereit et al. 2012). Hence, we attempt to examine whether the occurrences

of these two important blockings are linked to EISO-PJE and EISO-PJW. As a result, UB dominantly occurs in phases 8 and 1 of EISO-PJW, with 44.2% of all UB cases in the summers of 1982–2018 (Fig. 11a). LB, meanwhile, favors phases 7 and 8 of EISO-PJE, with 44.5% of all LB cases (Fig. 11b), and phases 5 and 6 of EISO-PJW, with 47.3% of all LB cases (Fig. 11c). Their remarkable linkages can be simply interpreted as follow: In the favorite phases for UB (i.e., phases 8 and 1 of EISO-PJW), EISO-PJW-associated high-pressure anomaly propagates across the Ural Mountains, strengthening the local meridional-type background flow in middle troposphere (Fig. S9a), which facilitates the formation of UB. Similarly, in the preferred phases for LB (i.e., phases 7 and 8 of EISO-PJE or phases 5 and 6 of EISO-PJW), the 500 hPa anomalous high pressure embedded
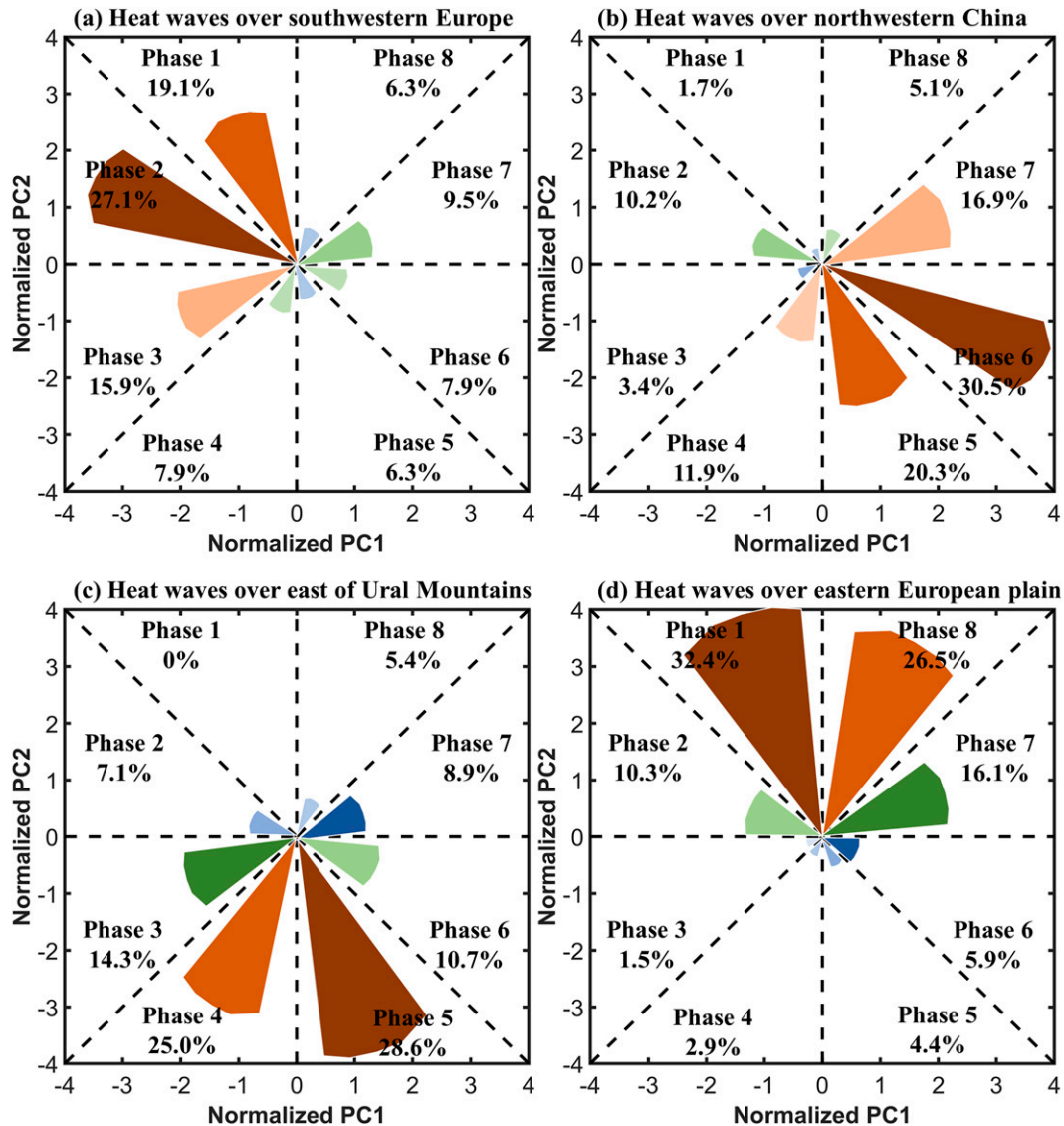
FIG. 10. The frequency of heatwaves in each phase based on (a) the EISO-SJE metric over southwestern Europe, (b) the EISO-SJE metric over northwestern China, (c) the EISO-PJE metric over the east of the Ural Mountains region, and (d) the EISO-PJW metric over the East European Plain.

in EISO-PJE or EISO-PJW promotes the meridional extension of the mean flow over the Lake Baikal region (Figs. S9b,c), which provides favorable conditions for the LB occurrences. These results suggest that EISOs can provide useful information for monitoring and predicting two important blockings, respectively, over the Ural Mountains and Lake Baikal.

5. Discussion

As the motivation of this study has been introduced in section 1, this study aims to objectively sort out and comprehensively clarify the dominant boreal summer EISOs over the Eurasian continent, and build up the real-time metrics for monitoring, subseasonal prediction, and model evaluation. In

terms of the dynamical essence for EISOs, we would give a brief discussion about their genesis in this section. From the perspective of the wave evolution associated with EISOs shown in Figs. 3, 5, and 7, EISO-SJE and EISO-PJE originate over the inlet of the Eurasian SJ and PJ regions, respectively. According to the previous work (e.g., Cai 1992; Cai et al. 2007; Zhu and Yang 2021), the entrance/exit region of the jet stream is characterized by the deformation flow caused by the strong zonal wind gradients. The deformation flow provides favorable conditions for converting energy from the mean flow to low-frequency intraseasonal eddies by barotropic instability (Lorenz 1972; Simmons et al. 1983; Frederiksen and Frederiksen 1997; Ding and Wang 2007). Recently, Dai et al. (2021) reported that the jet inlet/exit region tends to gain the
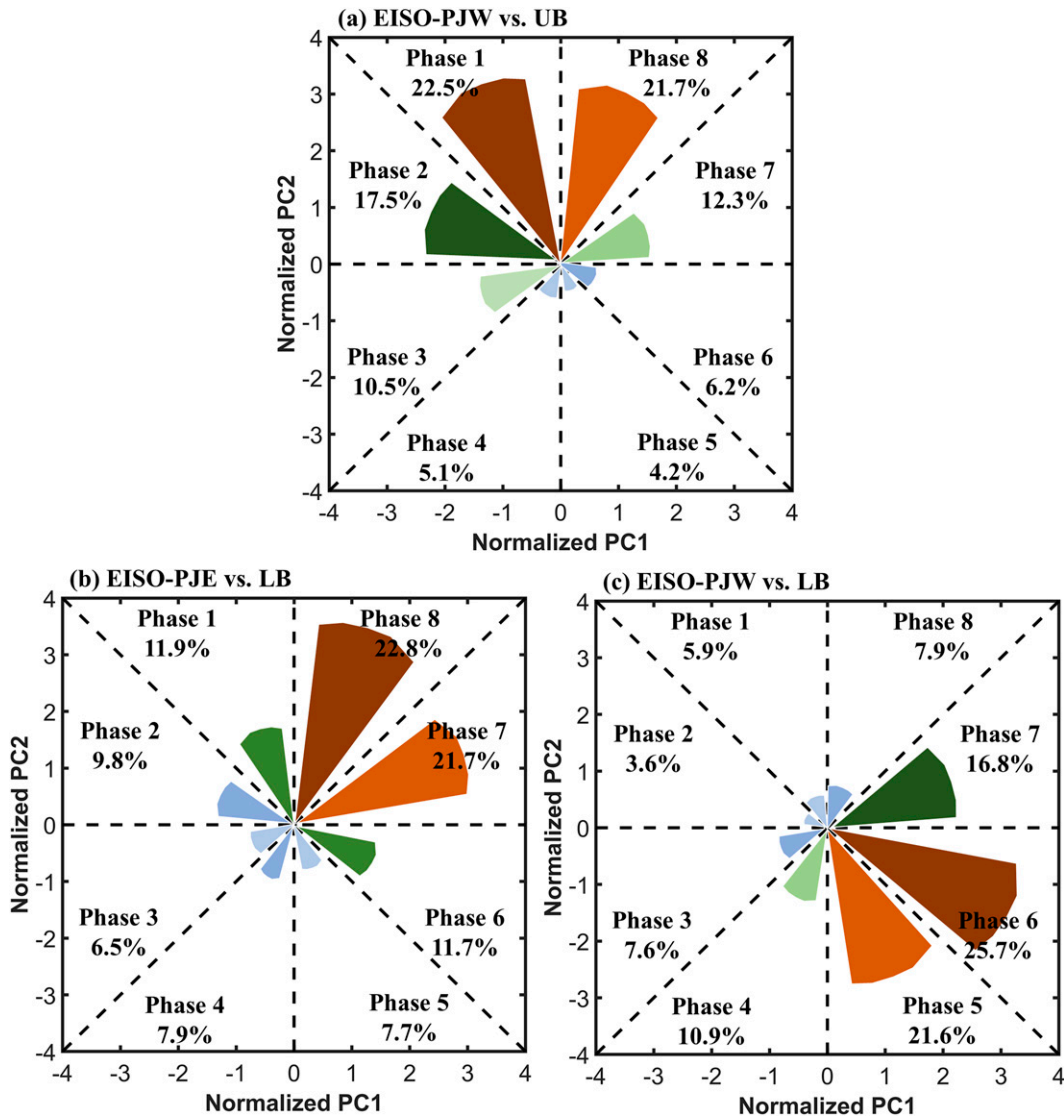
FIG. 11. (a) The frequency of UB in each phase based on the EISO-PJW metric. (b),(c) As in (a), but for LB based on the (b) EISO-PJE and (c) EISO-PJW metric.

low-frequency effective kinetic energy from the low-frequency available potential energy in lower troposphere by baroclinic instability, becoming a major source of low-frequency eddies. Therefore, the SJ and PJ inlet/exit regions facilitate the generation and intensification of intraseasonal perturbation, which propagates eastward along a waveguide of the westerly jet streams. Unlike EISO-SJE and EISO-PJE, EISO-PJW could be associated with the subpolar atmospheric internal variability, which could be a Rossby–Haurwitz wave reported by Branstator (1987). The westward propagation of EISO-PJW may be associated with the background weak upper-level westerly and even easterly in the subpolar region, as well as its longer wavelength. A deeper understanding about the dynamical mechanism of these three EISOs is worthwhile and will be given in another full study.

One concern is whether the EISOs portrayed in this study are independent of tropical ISOs because many previous studies have found that the tropical ISOs (including MJO and BSISO) modulate intraseasonal variation in extratropic (e.g., Lau and Phillips 1986; Mo and Kousky 1993; Kawamura et al. 1996; Cassou 2008; Wang et al. 2013; Lee et al. 2019; and many more). Purposely, we examine the concurrent evolution of tropical convection accompanied with the EISO strong events, and we cannot find any MJO/BSISO-like signals along with the evolution of these three EISOs (Fig. S10), which implies that tropical ISOs are not the forcing source of the jet-trapped intraseasonal waves. The above results further suggest that the boreal summer EISOs trapped in SJ and PJ may be primarily associated with mid- to high-latitude internal atmospheric dynamics.
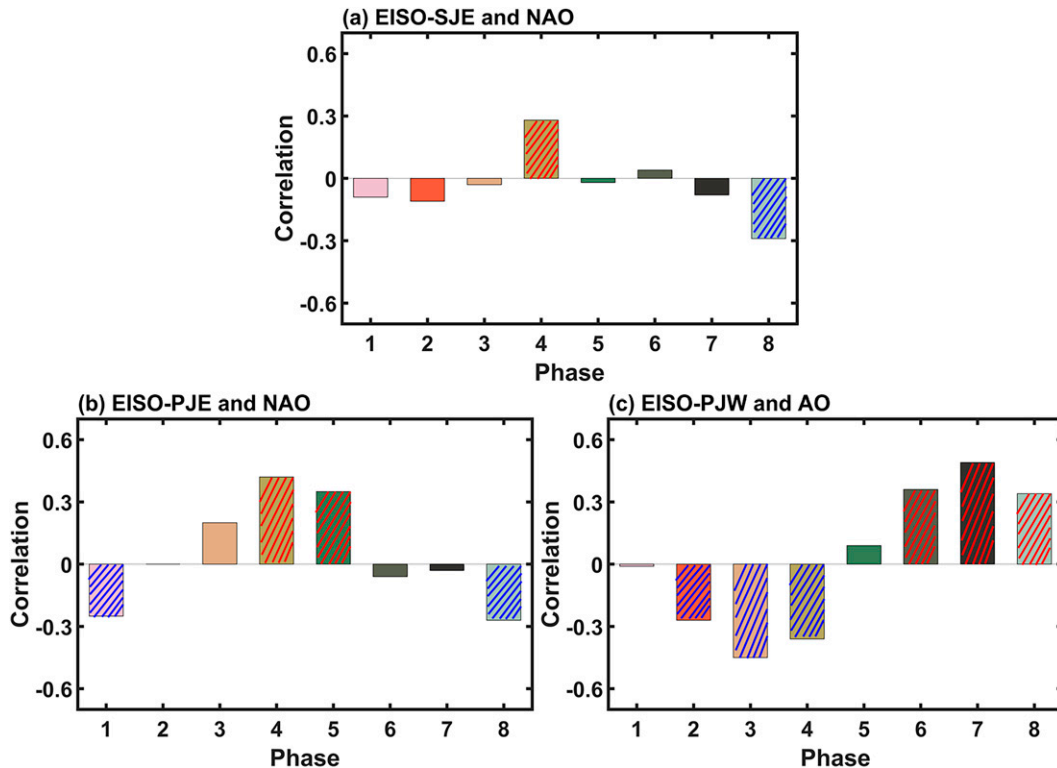
FIG. 12. (a) The spatial correlation between the EISO-SJE eight-phase composite 8–25-day GHT200 and 8–25-day NAO pattern. Hatched bars indicate the results are significant at the 95% confidence level. (b) As in (a), but for the spatial correlation between the EISO-PJE and 10–30-day NAO pattern. (c) As in (a), but for the spatial correlation between the EISO-PJW and 10–40-day AO pattern.

Another concern is whether the EISOs are connected with some well-known extratropical intraseasonal atmospheric circulation patterns. For example, North Atlantic Oscillation (NAO) and Arctic Oscillation (AO) are important atmospheric circulation patterns in the extratropical region (Hurrell 1995; Hurrell et al. 2003; Thompson and Wallace 1998, 2000; Wallace 2000), and both have evident subseasonal variations (Zhou and Miller 2005; Yadav and Straus 2017; Barnes et al. 2019). The relationships between the three EISOs and NAO or AO are examined. Following Li and Wang (2003a,b), the NAO domain is defined as (30°–80°N, 80°W–30°E), and the AO domain as (30°–90°N, 180°W–180°E). Figure 12a shows the spatial correlation between the NAO pattern and the eight-phase EISO-SJE pattern calculated over the NAO domain. Note that the NAO pattern is obtained by projecting the 8–25-day GHT200 onto the 8–25-day NAO index, and the EISO-SJE pattern is the eight-phase composite 8–25-day GHT200. As a result, the NAO has a significant relationship with EISO-SJE in phase 4 (with a correlation coefficient of 0.28) and phase 8 (with a correlation coefficient of −0.29). Similarly, EISO-PJE also has a close relationship with the NAO, in which the spatial correlation coefficient is significantly negative in phases 8 and 1, as well as significantly positive in phases 4 and 5 (Fig. 12b). Considering that NAO domain is located upstream of the EISO-SJE/EISO-PJE, the significant correlation between the NAO and EISO-SJE/

EISO-PJE in certain specific phases implies that the initiation of EISO-SJE/EISO-PJE may be related to the NAO subseasonal variation. According to Huang et al. (2020), NAO could excite the Rossby wave source via vortex stretching by abnormal divergence, which subsequently build the intraseasonal wave train over the Eurasian continent. Different from the relationship between the NAO and EISO-SJE/EISO-PJE, significant spatial correlations occur in most of the EISO-PJW phases (exclusion of phases 1 and 5) (Fig. 12c), which implies that the AO may impact the EISO-PJW's evolution. The above results suggest that NAO/AO may be the crucial factor in the initiation and evolution of the jet-trapped EISOs, and the relevant mechanisms are worthy of deep investigation in the future.

6. Summary and outlook

Using the historical data record (1982–2018), this study emphasizes the following two novelties. First, we objectively sort out and comprehensively clarify three dominant intraseasonal waves, respectively, along the SJ and PJ over the Eurasian continent during boreal summer. The behaviors of the three dominant intraseasonal waves are summarized schematically in Fig. 13. The first one, EISO-SJE, is retrieved by the first two EOF modes of the intraseasonal V200 over the SJ region (25°–55°N, 15°W–150°E). EISO-SJE features an 8–25-day periodicity and a zonal wavelength of about 4400 km between
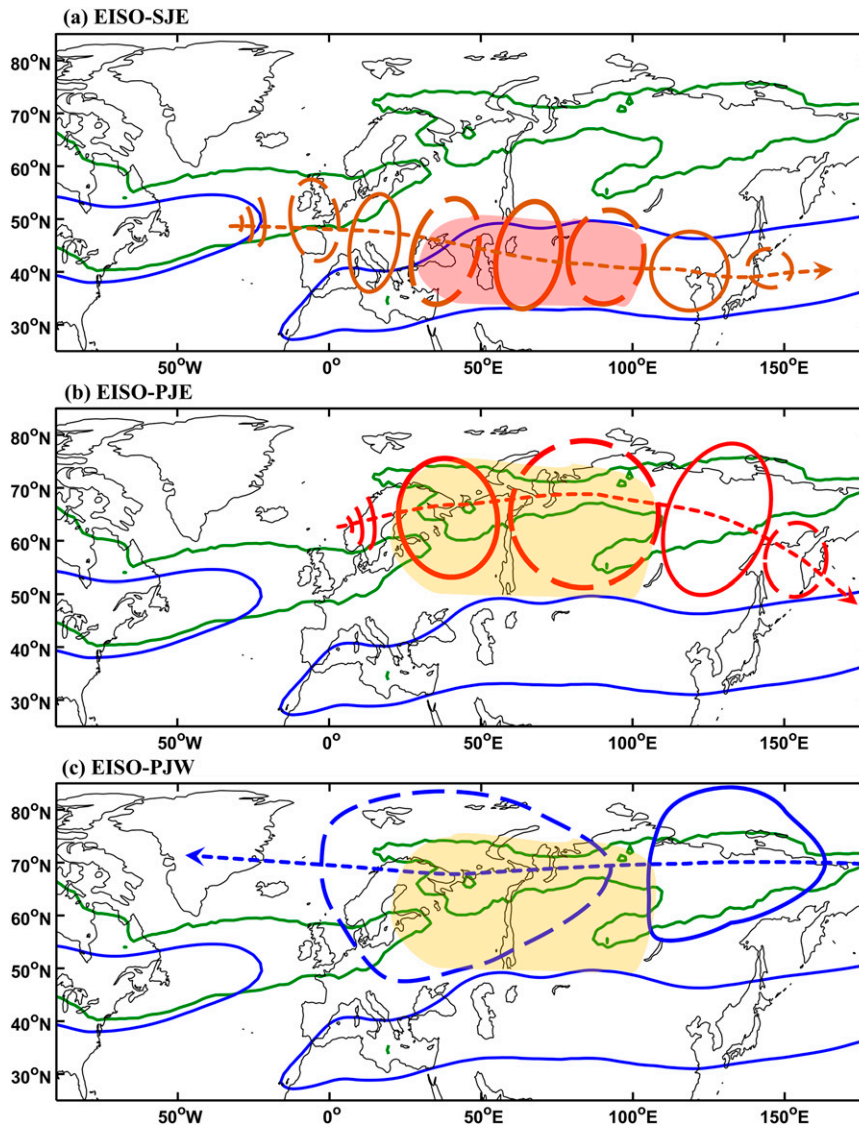
FIG. 13. Schematic diagram of (a) EISO-SJE, (b) EISO-PJE, and (c) EISO-PJW. The arrow shows the propagating direction, and the circles are the anomalous waves along the three types of EISOs based on Figs. 3, 5, and 7. Solid and dashed circles are positive and negative anomalies, respectively. The red shading in (a) represents the region of strengthening of EISO-SJE and the yellow shading in (b) and (c) represents the region of strengthening of the EISO-PJE and EISO-PJW. The blue and green contours denote the location of the boreal summer SJ and PJ, respectively.

25° and 55°N. It has a quasi-barotropic structure, initiates at the exit of the North America–North Atlantic jet core, and moves eastward with a phase speed of about 3.1 m s^{-1}, trapped along the subtropical jet stream over the Eurasian continent and with amplification over the Black Sea–Caspian Sea–arid central Asia area. The second one, EISO-PJE, is obtained by the first two EOF modes of the intraseasonal V250 over the PJ region (55°–85°N, 25°–150°E). EISO-PJE describes a high-latitude 10–30-day eastward-propagating wave with a quasi-barotropic structure and a zonal wavelength of about 4200 km. It initiates near Scandinavia, where the

bifurcation of the North America–North Atlantic jet and the PJ is situated, migrates eastward with a speed of 3.8 m s^{-1}, and enhances from the East European Plain, through the Ural Mountains, to the West Siberian Plain, before finally decays over the Okhotsk region. The third one, EISO-PJW, is represented by the first two EOF modes of the intraseasonal GHT250 over the same PJ region. EISO-PJW depicts a westward-migrating quasi-barotropic wave with a dominant periodicity of 10–40 days, wavelength of 5600 km, and speed of 4.0 m s^{-1} that enhances near the Ural Mountains and weakens over Scandinavia. It should be noted that the GHT anomalies

shown in phase 3 of EISO-SJE and phase 4 of EISO-PJE are partly similar to the Silk Road pattern (SRP; Lu et al. 2002) and British–Baikal Corridor pattern (BBC; Xu et al. 2019), respectively. Meanwhile, a recent work found that there is an eastward-propagating intraseasonal wave along the subtropical westerly jet affecting the East Asian rainfall pattern which is named as the intraseasonal SRP in consideration of geographical locations (Muetzelfeldt et al. 2023). Therefore, the EISO-SJE/EISO-PJE can be also called the intraseasonal SRP/BBC if emphasizing their geographical locations.

Second, the real-time EISO-SJE, EISO-PJE, and EISO-PJW metrics are also constructed by projecting the real-time running-mean processed V200*, V250*, and GHT250* onto the first two EOFs of EISO-SJE, EISO-PJE, and EISO-PJW patterns, respectively. The real-time EISO metrics do not use any future information and can be applied to operational real-time monitoring. The real-time EISO metrics cannot only capture the spatiotemporal features of three EISOs in application, but also clearly demonstrate the relationship between EISOs and heatwaves/blocking occurrence. The heatwaves over the southwestern Europe and northwestern China prefer phases 1–3 and phases 5 and 6 of EISO-SJE, respectively. The heatwaves over the east of the Ural Mountains area and East European Plain favor phases 4 and 5 of EISO-PJE and phases 8 and 1 of EISO-PJW, respectively. The UB preferably occurs in phases 8 and 1 of EISO-PJE, while LB favors phases 7 and 8 of EISO-PJE and phases 5 and 6 of EISO-PJW. Considering that the strong EISOs have long durations and at least one-third of EISO cases persist at least four phases, one can estimate the EISOs prior to 8–20 days based on the real-time EISO metrics and subsequently predict the probability of heatwaves and blockings in some hot regions at the S2S time scales.

Since this study focuses on the above two novelties, the dynamics of EISOs (e.g., energy analysis for EISOs' evolution and possible source) and their relations with some well-known tropical (MJO/BSISO) and extratropical signals (AO/NAO) are only briefly discussed in this study. Obviously, more deep physical mechanism is worthwhile to be investigated in the future, including how these intraseasonal waves are triggered, how EISOs interact with different components of the climate system, how the climate models replicate these intraseasonal modes, and how these modes affect the local subseasonal predictability.

REFERENCES

Annamalai, H., and J. M. Slingo, 2001: Active/break cycles: Diagnosis of the intraseasonal variability of the Asian summer monsoon. *Climate Dyn.*, **18**, 85–102, https://doi.org/10.1007/s003820100161.

Barnes, E. A., S. M. Samarasinghe, I. Ebert-Uphoff, and J. C. Furtado, 2019: Tropospheric and stratospheric causal pathways between the MJO and NAO. *J. Geophys. Res. Atmos.*, **124**, 9356–9371, https://doi.org/10.1029/2019JD031024.

Barriopedro, D., E. M. Fischer, J. Luterbacher, R. M. Trigo, and R. García-Herrera, 2011: The hot summer of 2010: Redrawing the temperature record map of Europe. *Science*, **332**, 220–224, https://doi.org/10.1126/science.1201224.

Beniston, M., and H. F. Diaz, 2004: The 2003 heat wave as an example of summers in a greenhouse climate? Observations and climate model simulations for Basel, Switzerland. *Global Planet. Change*, **44**, 73–81, https://doi.org/10.1016/j.gloplacha.2004.06.006.

Branstator, G., 1987: A striking example of the atmosphere's leading traveling pattern. *J. Atmos. Sci.*, **44**, 2310–2323, https://doi.org/10.1175/1520-0469(1987)044<2310:ASEOTA>2.0.CO;2.

——, 2002: Circumglobal teleconnections, the jet stream waveguide, and the North Atlantic Oscillation. *J. Climate*, **15**, 1893–1910, https://doi.org/10.1175/1520-0442(2002)015<1893:CTTJSW>2.0.CO;2.

Cai, M., 1992: A physical interpretation for the stability property of a localized disturbance in a deformation flow. *J. Atmos. Sci.*, **49**, 2177–2182, https://doi.org/10.1175/1520-0469(1992)049<2177:APIFTS>2.0.CO;2.

——, S. Yang, H. van den Dool, and V. E. Kousky, 2007: Dynamical implications of the orientation of atmospheric eddies: A local energetics perspective. *Tellus*, **59A**, 127–140, https://doi.org/10.1111/j.1600-0870.2006.00213.x.

Cassou, C., 2008: Intraseasonal interaction between the Madden–Julian oscillation and the North Atlantic Oscillation. *Nature*, **455**, 523–527, https://doi.org/10.1038/nature07286.

Chan, J. C. L., W. Ai, and J. Xu, 2002: Mechanisms responsible for the maintenance of the 1998 South China Sea summer monsoon. *J. Meteor. Soc. Japan*, **80**, 1103–1113, https://doi.org/10.2151/jmsj.80.1103.

Chauvin, F., R. Roehrig, and J.-P. Lafore, 2010: Intraseasonal variability of the Saharan heat low and its link with midlatitudes. *J. Climate*, **23**, 2544–2561, https://doi.org/10.1175/2010JCLI3093.1.

Chen, Y., and P. Zhai, 2017: Simultaneous modulations of precipitation and temperature extremes in southern parts of China by the boreal summer intraseasonal oscillation. *Climate Dyn.*, **49**, 3363–3381, https://doi.org/10.1007/s00382-016-3518-4.

Cheng, Y., L. Wang, and T. Li, 2021: Two distinct types of 10–30-day persistent heavy rainfall events over the Yangtze River Valley. *J. Climate*, **34**, 9571–9584, https://doi.org/10.1175/JCLI-D-20-0741.1.

Dai, X., Y. Zhang, and X. Yang, 2021: The budget of local available potential energy of low-frequency eddies in Northern Hemispheric winter. *J. Climate*, **34**, 1241–1258, https://doi.org/10.1175/JCLI-D-19-1007.1.

Dee, D. P., and Coauthors, 2011: The ERA-Interim reanalysis: Configuration and performance of the data assimilation

system. *Quart. J. Roy. Meteor. Soc.*, **137**, 553–597, https://doi.org/10.1002/qj.828.

Diao, Y., J. Li, and D. Luo, 2006: A new blocking index and its application: Blocking action in the Northern Hemisphere. *J. Climate*, **19**, 4819–4839, https://doi.org/10.1175/JCLI3886.1.

Dickey, J. O., M. Ghil, and S. L. Marcus, 1991: Extratropical aspects of the 40–50 day oscillation in length-of-day and atmospheric angular momentum. *J. Geophys. Res.*, **96**, 22 643–22 658, https://doi.org/10.1029/91JD02339.

Ding, Q., and B. Wang, 2005: Circumglobal teleconnection in the Northern Hemisphere summer. *J. Climate*, **18**, 3483–3505, https://doi.org/10.1175/JCLI3473.1.

——, and ——, 2007: Intraseasonal teleconnection between the summer Eurasian wave train and the Indian monsoon. *J. Climate*, **20**, 3751–3767, https://doi.org/10.1175/JCLI4221.1.

Du, L., and R. Lu, 2021: Wave trains of 10–30-day meridional wind variations over the North Pacific during summer. *J. Climate*, **34**, 9267–9277, https://doi.org/10.1175/JCLI-D-21-0096.1.

Dugam, S. S., S. D. Bansod, and S. B. Kakade, 2009: Pre-monsoon zonal wind Index over Tibetan Plateau and sub-seasonal Indian summer monsoon rainfall variability. *Geophys. Res. Lett.*, **36**, L11809, https://doi.org/10.1029/2009GL038207.

Ferranti, L., T. N. Palmer, F. Molteni, and E. Klinker, 1990: Tropical-extratropical interaction associated with the 30–60 day oscillation and its impact on medium and extended range prediction. *J. Atmos. Sci.*, **47**, 2177–2199, https://doi.org/10.1175/1520-0469(1990)047<2177:TEIAWT>2.0.CO;2.

Frederiksen, J. S., and P. J. Webster, 1988: Alternative theories of atmospheric teleconnections and low-frequency fluctuations. *Rev. Geophys.*, **26**, 459–494, https://doi.org/10.1029/RG026i003p00459.

——, and C. S. Frederiksen, 1997: Mechanism of the formation of intraseasonal oscillations and Australian monsoon disturbances: The roles of convection, barotropic and baroclinic instability. *Contrib. Atmos. Phys.*, **70**, 39–56.

Fujinami, H., and T. Yasunari, 2004: Submonthly variability of convection and circulation over and around the Tibetan Plateau during the boreal summer. *J. Meteor. Soc. Japan*, **82**, 1545–1564, https://doi.org/10.2151/jmsj.82.1545.

Gao, M., J. Yang, B. Wang, S. Zhou, D. Gong, and S.-J. Kim, 2018: How are heat waves over Yangtze River Valley associated with atmospheric quasi-biweekly oscillation? *Climate Dyn.*, **51**, 4421–4437, https://doi.org/10.1007/s00382-017-3526-z.

Gao, Y., P.-C. Hsu, S. Che, C. Yu, and S. Han, 2022: Origins of intraseasonal precipitation variability over North China in the rainy season. *J. Climate*, **35**, 6219–6236, https://doi.org/10.1175/JCLI-D-21-0832.1.

Garfinkel, C. I., J. J. Benedict, and E. D. Maloney, 2014: Impact of the MJO on the boreal winter extratropical circulation. *Geophys. Res. Lett.*, **41**, 6055–6062, https://doi.org/10.1002/2014GL061094.

Ghil, M., and K. Mo, 1991: Intraseasonal oscillations in the global atmosphere. Part I: Northern Hemisphere and tropics. *J. Atmos. Sci.*, **48**, 752–779, https://doi.org/10.1175/1520-0469(1991)048<0752:IOITGA>2.0.CO;2.

Giannakaki, P., and O. Martius, 2016: An object-based forecast verification tool for synoptic-scale Rossby waveguides. *Wea. Forecasting*, **31**, 937–946, https://doi.org/10.1175/WAF-D-15-0147.1.

Gilman, D. L., F. J. Fuglister, and J. M. Mitchell Jr., 1963: On the power spectrum of "red noise." *J. Atmos. Sci.*, **20**, 182–184, https://doi.org/10.1175/1520-0469(1963)020<0182:OTPSON>2.0.CO;2.

Hannachi, A., D. M. Straus, C. L. E. Franzke, S. Corti, and T. Woollings, 2017: Low-frequency nonlinearity and regime behavior in the Northern Hemisphere extratropical atmosphere. *Rev. Geophys.*, **55**, 199–234, https://doi.org/10.1002/2015RG000509.

He, B., P. Liu, Y. Zhu, and W. Hu, 2019: Prediction and predictability of Northern Hemisphere persistent maxima of 500-hPa geopotential height eddies in the GEFS. *Climate Dyn.*, **52**, 3773–3789, https://doi.org/10.1007/s00382-018-4347-4.

Hendon, H. H., and B. Liebmann, 1990: The intraseasonal (30–50 day) oscillation of the Australian summer monsoon. *J. Atmos. Sci.*, **47**, 2909–2924, https://doi.org/10.1175/1520-0469(1990)047<2909:TIDOOT>2.0.CO;2.

Hoskins, B., 2013: The potential for skill across the range of the seamless weather-climate prediction problem: A stimulus for our science. *Quart. J. Roy. Meteor. Soc.*, **139**, 573–584, https://doi.org/10.1002/qj.1991.

——, I. N. James, and G. H. White, 1983: The shape, propagation and mean-flow interaction of large-scale weather systems. *J. Atmos. Sci.*, **40**, 1595–1612, https://doi.org/10.1175/1520-0469(1983)040<1595:TSPAMF>2.0.CO;2.

Hsu, P.-C., T. Li, L. You, J. Gao, and H.-L. Ren, 2015: A spatial-temporal projection model for 10-30 day rainfall forecast in South China. *Climate Dyn.*, **44**, 1227–1244, https://doi.org/10.1007/s00382-014-2215-4.

Hu, K., G. Huang, R. Wu, and L. Wang, 2018: Structure and dynamics of a wave train along the wintertime Asian jet and its impact on East Asian climate. *Climate Dyn.*, **51**, 4123–4137, https://doi.org/10.1007/s00382-017-3674-1.

Huang, D.-Q., J. Zhu, Y.-C. Zhang, and A.-N. Huang, 2014: The different configurations of the East Asian polar front jet and subtropical jet and the associated rainfall anomalies over eastern China in summer. *J. Climate*, **27**, 8205–8220, https://doi.org/10.1175/JCLI-D-14-00067.1.

Huang, S., X. Li, and Z. Wen, 2020: Characteristics and possible sources of the intraseasonal South Asian jet wave train in boreal winter. *J. Climate*, **33**, 10 523–10 537, https://doi.org/10.1175/JCLI-D-20-0125.1.

Hurrell, J. W., 1995: Decadal trends in the North Atlantic Oscillation: Regional temperatures and precipitation. *Science*, **269**, 676–679, https://doi.org/10.1126/science.269.5224.676.

——, Y. Kushnir, G. Ottersen, and M. Visbeck, 2003: *An overview of the North Atlantic Oscillation. Geophys. Monogr.*, Vol. 134, Amer. Geophys. Union, 35 pp., https://doi.org/10.1029/134GM01.

Iwao, K., and M. Takahashi, 2008: A precipitation seesaw mode between northeast Asia and Siberia in summer caused by Rossby waves over the Eurasian continent. *J. Climate*, **21**, 2401–2419, https://doi.org/10.1175/2007JCLI1949.1.

Jiang, X., T. Li, and B. Wang, 2004: Structures and mechanisms of the northward propagating boreal summer intraseasonal oscillation. *J. Climate*, **17**, 1022–1039, https://doi.org/10.1175/1520-0442(2004)017<1022:SAMOTN>2.0.CO;2.

Kautz, L.-A., O. Martius, S. Pfahl, J. G. Pinto, A. M. Ramos, P. M. Sousa, and T. Woollings, 2022: Atmospheric blocking and weather extremes over the Euro-Atlantic sector–a review. *Wea. Climate Dyn.*, **3**, 305–336, https://doi.org/10.5194/wcd-3-305-2022.

Kawamura, R., T. Murakami, and B. Wang, 1996: Tropical and midlatitude 45-day perturbations over the western Pacific during the northern summer. *J. Meteor. Soc. Japan*, **74**, 867–890, https://doi.org/10.2151/jmsj1965.74.6_867.

Kemball-Cook, S., and B. Wang, 2001: Equatorial waves and air–sea interaction in the boreal summer intraseasonal oscillation. *J. Climate*, **14**, 2923–2942, https://doi.org/10.1175/1520-0442(2001)014<2923:EWAASI>2.0.CO;2.

Kikuchi, K., B. Wang, and Y. Kajikawa, 2012: Bimodal representation of the tropical intraseasonal oscillation. *Climate Dyn.*, **38**, 1989–2000, https://doi.org/10.1007/s00382-011-1159-1.

Kornhuber, K., D. Coumou, E. Vogel, C. Lesk, J. F. Donges, J. Lehmann, and R. Horton, 2020: Amplified Rossby waves enhance risk of concurrent heatwaves in major breadbasket regions. *Nat. Climate Change*, **10**, 48–53, https://doi.org/10.1038/s41558-019-0637-z.

Kosaka, Y., and H. Nakamura, 2006: Structure and dynamics of the summertime Pacific–Japan teleconnection pattern. *Quart. J. Roy. Meteor. Soc.*, **132**, 2009–2030, https://doi.org/10.1256/qj.05.204.

——, and ——, 2010: Mechanisms of meridional teleconnection observed between a summer monsoon system and a subtropical anticyclone. Part I: The Pacific–Japan pattern. *J. Climate*, **23**, 5085–5108, https://doi.org/10.1175/2010JCLI3413.1.

Kueh, M.-T., and C.-Y. Lin, 2020: The 2018 summer heatwaves over northwestern Europe and its extended-range prediction. *Sci. Rep.*, **10**, 19283, https://doi.org/10.1038/s41598-020-76181-4.

Lau, K.-M., and T. J. Phillips, 1986: Coherent fluctuations of extratropical geopotential height and tropical convection in intraseasonal time scales. *J. Atmos. Sci.*, **43**, 1164–1181, https://doi.org/10.1175/1520-0469(1986)043<1164:CFOFGH>2.0.CO;2.

Lee, J.-Y., B. Wang, M. C. Wheeler, X. Fu, D. E. Waliser, and I.-S. Kang, 2013: Real-time multivariate indices for the boreal summer intraseasonal oscillation over the Asian summer monsoon region. *Climate Dyn.*, **40**, 493–509, https://doi.org/10.1007/s00382-012-1544-4.

Lee, R. W., S. J. Woolnough, A. J. Charlton-Perez, and F. Vitart, 2019: ENSO modulation of MJO teleconnections to the North Atlantic and Europe. *Geophys. Res. Lett.*, **46**, 13 535–13 545, https://doi.org/10.1029/2019GL084683.

Lee, S., 1997: Maintenance of multiple jets in a baroclinic flow. *J. Atmos. Sci.*, **54**, 1726–1738, https://doi.org/10.1175/1520-0469(1997)054<1726:MOMJIA>2.0.CO;2.

Lejenäs, H., and H. Økland, 1983: Characteristics of Northern Hemisphere blocking as determined from a long time series of observational data. *Tellus*, **35A**, 350–362, https://doi.org/10.3402/tellusa.v35i5.11446.

Lenggenhager, S., M. Croci-Maspoli, S. Bronnimann, and O. Martius, 2019: On the dynamical coupling between atmospheric blocks and heavy precipitation events: A discussion of the southern Alpine flood in October 2000. *Quart. J. Roy. Meteor. Soc.*, **145**, 530–545, https://doi.org/10.1002/qj.3449.

Li, C., 1990: Intraseasonal oscillation in the atmosphere (in Chinese). *Chin. J. Atmos. Sci.*, **14**, 32–45.

——, 1991: Global characteristics of 30-60 day atmospheric oscillation (in Chinese). *Chin. J. Atmos. Sci.*, **15**, 66–76.

Li, J., and J. X. L. Wang, 2003a: A new North Atlantic oscillation index and its variability. *Adv. Atmos. Sci.*, **20**, 661–676, https://doi.org/10.1007/BF02915394.

——, and ——, 2003b: A modified zonal index and its physical sense. *Geophys. Res. Lett.*, **30**, 1632, https://doi.org/10.1029/2003GL017441.

——, P. Zhai, J. Mao, L. Song, and Q. Xiao, 2021: Synergistic effect of the 25-60-day tropical and midlatitude intraseasonal oscillations on the persistently severe Yangtze floods. *Geophys. Res. Lett.*, **48**, e2021GL095129, https://doi.org/10.1029/2021GL095129.

Liebmann, B., H. H. Hendon, and J. D. Glick, 1994: The relationship between tropical cyclones of the western Pacific and Indian Oceans and the Madden-Julian Oscillation. *J. Meteor. Soc. Japan*, **72**, 401–412, https://doi.org/10.2151/jmsj1965.72.3_401.

Lin, H., 2013: Monitoring and predicting the intraseasonal variability of the East Asian–western North Pacific summer monsoon. *Mon. Wea. Rev.*, **141**, 1124–1138, https://doi.org/10.1175/MWR-D-12-00087.1.

Liu, B., Y. Yan, C. Zhu, S. Ma, and J. Li, 2020: Record-breaking meiyu rainfall around the Yangtze River in 2020 regulated by the subseasonal phase transition of the North Atlantic oscillation. *Geophys. Res. Lett.*, **47**, e2020GL090342, https://doi.org/10.1029/2020GL090342.

Liu, H.-B., J. Yang, D.-L. Zhang, and B. Wang, 2014: Roles of synoptic to quasi-biweekly disturbances in generating the summer 2003 heavy rainfall in East China. *Mon. Wea. Rev.*, **142**, 886–904, https://doi.org/10.1175/MWR-D-13-00055.1.

Liu, L., L. Sun, Y. Liao, Y. Zhu, X. Zou, Y. Wang, and J. Yan, 2008: Development and application of national prediction system for extreme high temperature (in Chinese). *Meteor. Mon.*, **34**, 102–107.

Liu, P., and Coauthors, 2018: Climatology of tracked persistent maxima of 500-hPa geopotential height. *Climate Dyn.*, **51**, 701–717, https://doi.org/10.1007/s00382-017-3950-0.

Lorenz, E. N., 1972: Barotropic instability of Rossby wave motion. *J. Atmos. Sci.*, **29**, 258–265, https://doi.org/10.1175/1520-0469(1972)029<0258:BIORWM>2.0.CO;2.

Lu, R.-Y., J.-H. Oh, and B.-J. Kim, 2002: A teleconnection pattern in upper-level meridional wind over the North African and Eurasian continent in summer. *Tellus*, **54A**, 44–55, https://doi.org/10.3402/tellusa.v54i1.12122.

Lu, R., Z. Lin, and Y. Zhang, 2013: Variability of the East Asian upper-tropospheric jet in summer and its impacts on the East Asian monsoon (in Chinese). *Chin. J. Atmos. Sci.*, **37**, 331–340.

Madden, R. A., and P. R. Julian, 1971: Detection of a 40–50 day oscillation in the zonal wind in the tropical Pacific. *J. Atmos. Sci.*, **28**, 702–708, https://doi.org/10.1175/1520-0469(1971)028<0702:DOADOI>2.0.CO;2.

——, and ——, 1972: Description of global-scale circulation cells in the tropics with a 40–50 day period. *J. Atmos. Sci.*, **29**, 1109–1123, https://doi.org/10.1175/1520-0469(1972)029<1109:DOGSCC>2.0.CO;2.

Maloney, E. D., and D. L. Hartmann, 2000: Modulation of eastern North Pacific hurricanes by the Madden-Julian oscillation. *J. Climate*, **13**, 1451–1460, https://doi.org/10.1175/1520-0442(2000)013<1451:MOENPH>2.0.CO;2.

——, and ——, 2001: The Madden–Julian oscillation, barotropic dynamics, and North Pacific tropical cyclone formation. Part I: Observations. *J. Atmos. Sci.*, **58**, 2545–2558, https://doi.org/10.1175/1520-0469(2001)058<2545:TMJOBD>2.0.CO;2.

Martius, O., C. Schwierz, and H. C. Davies, 2010: Tropopause-level waveguides. *J. Atmos. Sci.*, **67**, 866–879, https://doi.org/10.1175/2009JAS2995.1.

Mo, K. C., and V. E. Kousky, 1993: Further analysis of the relationship between circulation anomaly patterns and tropical convection. *J. Geophys. Res.*, **98**, 5103–5113, https://doi.org/10.1029/92JD02952.

Muetzelfeldt, M. R., R. Schiemann, A. G. Turner, P. L. Vidale, and A. Menon, 2023: Intraseasonal oscillations of the Silk Road pattern lead to predictability in East Asian precipitation

patterns and the Mei Yu front. *Environ. Res. Commun.*, **5**, 015003, https://doi.org/10.1088/2515-7620/acb040.

Namias, J., 1950: The index cycle and its role in the general circulation. *J. Meteor. Sci.*, **7**, 130–139, https://doi.org/10.1175/1520-0469(1950)007<0130:TICAIR>2.0.CO;2.

North, G. R., T. L. Bell, R. F. Cahalan, and F. J. Moeng, 1982: Sampling errors in the estimation of empirical orthogonal functions. *Mon. Wea. Rev.*, **110**, 699–706, https://doi.org/10.1175/1520-0493(1982)110<0699:SEITEO>2.0.CO;2.

Panetta, R. L., 1993: Zonal jets in wide baroclinically unstable regions: Persistence and scale selection. *J. Atmos. Sci.*, **50**, 2073–2106, https://doi.org/10.1175/1520-0469(1993)050<2073:ZJIWBU>2.0.CO;2.

Qi, X., and J. Yang, 2019: Extended-range prediction of a heat wave event over the Yangtze River Valley: Role of intraseasonal signals. *Atmos. Oceanic Sci. Lett.*, **12**, 451–457, https://doi.org/10.1080/16742834.2019.1669408.

——, ——, M. Gao, H. Yang, and H. Liu, 2019: Roles of the tropical/extratropical intraseasonal oscillations on generating the heat wave over Yangtze River Valley: A numerical study. *J. Geophys. Res. Atmos.*, **124**, 3110–3123, https://doi.org/10.1029/2018JD029868.

Qian, Y., P.-C. Hsu, and K. Kazuyoshi, 2019: New real-time indices for the quasi-biweekly oscillation over the Asian summer monsoon region. *Climate Dyn.*, **53**, 2603–2624, https://doi.org/10.1007/s00382-019-04644-0.

Robertson, A. W., A. Kumar, M. Pea, and F. Vitart, 2015: Improving and promoting subseasonal to seasonal prediction. *Bull. Amer. Meteor. Soc.*, **96**, ES49–ES53, https://doi.org/10.1175/BAMS-D-14-00139.1.

Robine, J., S. Cheung, S. Roy, H. Oyen, C. Griffiths, J. Michel, and F. Herrmann, 2008: Death toll exceeded 70,000 in Europe during the summer of 2003. *C. R. Biol.*, **331**, 171–178, https://doi.org/10.1016/j.crvi.2007.12.001.

Rodrigues, R. R., A. S. Taschetto, A. S. Gupta, and G. R. Foltz, 2019: Common cause for severe droughts in South America and marine heatwaves in the South Atlantic. *Nat. Geosci.*, **12**, 620–626, https://doi.org/10.1038/s41561-019-0393-8.

Sanchez-Gomez, E., L. Terray, and B. Joly, 2008: Intra-seasonal atmospheric variability and extreme precipitation events in the European-Mediterranean region. *Geophys. Res. Lett.*, **35**, L15708, https://doi.org/10.1029/2008GL034515.

Sato, N., and M. Takahashi, 2003: Formation mechanism of vorticity anomalies on the subtropical jet in the midsummer Northern Hemisphere. *Theor. Appl. Mech. Japan*, **52**, 109–115.

Schneidereit, A., S. Schubert, P. Vargin, F. Lunkeit, X. Zhu, D. H. W. Peters, and K. Fraedrich, 2012: Large-scale flow and the long-lasting blocking high over Russia: Summer 2010. *Mon. Wea. Rev.*, **140**, 2967–2981, https://doi.org/10.1175/MWR-D-11-00249.1.

Schubert, S., H. Wang, and M. Suarez, 2011: Warm season subseasonal variability and climate extremes in the Northern Hemisphere: The role of stationary Rossby waves. *J. Climate*, **24**, 4773–4792, https://doi.org/10.1175/JCLI-D-10-05035.1.

Simmons, A. J., J. M. Wallace, and G. W. Branstator, 1983: Barotropic wave propagation and instability, and atmospheric teleconnection patterns. *J. Atmos. Sci.*, **40**, 1363–1392, https://doi.org/10.1175/1520-0469(1983)040<1363:BWPAIA>2.0.CO;2.

Stan, C., and V. Krishnamurthy, 2019: Intra-seasonal and seasonal variability of the Northern Hemisphere extra-tropics. *Climate Dyn.*, **53**, 4821–4839, https://doi.org/10.1007/s00382-019-04827-9.

——, D. M. Straus, J. S. Frederiksen, H. Lin, E. D. Maloney, and C. Schumacher, 2017: Review of tropical-extratropical teleconnections on intraseasonal time scales. *Rev. Geophys.*, **55**, 902–937, https://doi.org/10.1002/2016RG000538.

Straus, D. M., E. Swenson, and C.-L. Lappen, 2015: The MJO cycle forcing of the North Atlantic circulation: Intervention experiments with the Community Earth System Model. *J. Atmos. Sci.*, **72**, 660–681, https://doi.org/10.1175/JAS-D-14-0145.1.

Sultan, B., S. Janicot, and A. Diedhiou, 2003: The West African monsoon dynamics. Part I: Documentation of intraseasonal variability. *J. Climate*, **16**, 3389–3406, https://doi.org/10.1175/1520-0442(2003)016<3389:TWAMDP>2.0.CO;2.

Sun, X., S. Li, J. Sun, and X. Hong, 2018: Differences in intraseasonal activity of Eurasian Subtropical zonal wave train and associated Indian summer rainfall in two opposite AMO phases. *Chin. J. Atmos. Sci.*, **42**, 1067–1080, https://doi.org/10.3878/j.issn.1006-9895.1712.17177.

Tang, Y., G. Zeng, X. Yang, V. Lyakaremye, and Z. Li, 2022: Intraseasonal oscillation of summer extreme high temperature in northeast China and associated atmospheric circulation anomalies. *Atmosphere*, **13**, 387, https://doi.org/10.3390/atmos13030387.

Teng, H., G. Branstator, H. Wang, G. A. Meehl, and W. M. Washington, 2013: Probability of US heat waves affected by a subseasonal planetary wave pattern. *Nat. Geosci.*, **6**, 1056–1061, https://doi.org/10.1038/ngeo1988.

Thompson, D. W. J., and J. M. Wallace, 1998: The Arctic Oscillation signature in the wintertime geopotential height and temperature fields. *Geophys. Res. Lett.*, **25**, 1297–1300, https://doi.org/10.1029/98GL00950.

——, and ——, 2000: Annular modes in the extratropical circulation. Part I: Month-to-month variability. *J. Climate*, **13**, 1000–1016, https://doi.org/10.1175/1520-0442(2000)013<1000:AMITEC>2.0.CO;2.

Tibaldi, S., and F. Molteni, 1990: On the operational predictability of blocking. *Tellus*, **42A**, 343–365, https://doi.org/10.3402/tellusa.v42i3.11882.

Tomczyk, A. M., M. Polrolniczak, and E. Bednorz, 2017: Circulation conditions' effect on the occurrence of heat waves in western and southwestern Europe. *Atmosphere*, **8**, 31, https://doi.org/10.3390/atmos8020031.

Tyrlis, E., and B. J. Hoskins, 2008: Aspects of a Northern Hemisphere atmospheric blocking climatology. *J. Atmos. Sci.*, **65**, 1638–1652, https://doi.org/10.1175/2007JAS2337.1.

Vitart, F., C. Ardilouze, A. Bonet, A. Brookshaw, M. Chen, C. Codorean, and L. Zhang, 2017: The Subseasonal to Seasonal (S2S) Prediction project database. *Bull. Amer. Meteor. Soc.*, **98**, 163–173, https://doi.org/10.1175/BAMS-D-16-0017.1.

Wallace, J. M., 2000: North Atlantic oscillation/annular mode: Two paradigms-one phenomenon. *Quart. J. Roy. Meteor. Soc.*, **126**, 791–805, https://doi.org/10.1256/smsqj.56401.

Wang, B., and X. Xie, 1997: A model for the boreal summer intraseasonal oscillation. *J. Atmos. Sci.*, **54**, 72–86, https://doi.org/10.1175/1520-0469(1997)054<0072:AMFTBS>2.0.CO;2.

Wang, H., F. Liu, B. Wang, G. Chen, and W. Dong, 2021: Diversity of intraseasonal oscillation over the western North Pacific. *Climate Dyn.*, **57**, 1881–1893, https://doi.org/10.1007/s00382-021-05780-2.

Wang, J., 2020: Relationships between Jianghuai Meiyu anomaly and the collaborative evolution of wave trains in the upper and lower troposphere in mid-July of 2020. *Front. Earth Sci.*, **8**, 597930, https://doi.org/10.3389/feart.2020.597930.

Wang, L., T. Li, T. Zhou, and X. Rong, 2013: Origin of the intraseasonal variability over the North Pacific in boreal summer. *J. Climate*, **26**, 1211–1229, https://doi.org/10.1175/JCLI-D-11-00704.1.

Wang, P., J. Tang, S. Wang, X. Dong, and J. Fang, 2017: Regional heatwaves in China: A cluster analysis. *Climate Dyn.*, **50**, 1919–1925, https://doi.org/10.1007/s00382-017-3815-6.

Wheeler, M. C., and H. H. Hendon, 2004: An all-season real-time multivariate MJO index: Development of an index for monitoring and prediction. *Mon. Wea. Rev.*, **132**, 1917–1932, https://doi.org/10.1175/1520-0493(2004)132<1917:AARMMI>2.0.CO;2.

White, R. H., K. Kornhuber, O. Martius, and V. Wirth, 2022: From atmospheric waves to heatwaves: A waveguide perspective for understanding and predicting concurrent, persistent, and extreme extratropical weather. *Bull. Amer. Meteor. Soc.*, **103**, E923–E935, https://doi.org/10.1175/BAMS-D-21-0170.1.

Wirth, V., M. Riemer, E. K. M. Chang, and O. Martius, 2018: Rossby wave packets on the midlatitude waveguide—A review. *Mon. Wea. Rev.*, **146**, 1965–2001, https://doi.org/10.1175/MWR-D-16-0483.1.

Wu, J., H.-L. Ren, P. Zhang, Y. Wang, Y. Liu, C. Zhao, and Q. Li, 2022: The dynamical-statistical subseasonal prediction of precipitation over China based on the BCC new-generation coupled model. *Climate Dyn.*, **59**, 1213–1232, https://doi.org/10.1007/s00382-022-06187-3.

Xu, P., L. Wang, and W. Chen, 2019: The British–Baikal corridor: A teleconnection pattern along the summertime polar front jet over Eurasia. *J. Climate*, **32**, 877–896, https://doi.org/10.1175/JCLI-D-18-0343.1.

——, ——, ——, G. Chen, and I.-S. Kang, 2020: Intraseasonal variations of the British–Baikal corridor pattern. *J. Climate*, **33**, 2183–2200, https://doi.org/10.1175/JCLI-D-19-0458.1.

Yadav, P., and D. M. Straus, 2017: Circulation response to fast and slow MJO episodes. *Mon. Wea. Rev.*, **145**, 1577–1596, https://doi.org/10.1175/MWR-D-16-0352.1.

Yan, Y., B. Liu, and C. Zhu, 2021a: Subseasonal predictability of South China Sea summer monsoon onset with the ECMWF S2S forecasting system. *Geophys. Res. Lett.*, **48**, e2021GL095943, https://doi.org/10.1029/2021GL095943.

——, ——, ——, R. Lu, N. Jiang, and S. Ma, 2021b: Subseasonal forecast barrier of the North Atlantic oscillation in S2S models during the extreme mei-yu rainfall event in 2020. *Climate Dyn.*, **58**, 2913–2925, https://doi.org/10.1007/s00382-021-06076-1.

Yang, J., B. Wang, and B. Wang, 2008: Anticorrelated intensity change of the quasi-biweekly and 30–50-day oscillations over the South China Sea. *Geophys. Res. Lett.*, **35**, L16702, https://doi.org/10.1029/2008GL034449.

——, Q. Bao, B. Wang, D.-Y. Gong, H. He, and M.-N. Gao, 2014: Distinct quasi-biweekly features of the subtropical East Asian monsoon during early and late summers. *Climate Dyn.*, **42**, 1469–1486, https://doi.org/10.1007/s00382-013-1728-6.

——, ——, ——, D. Y. Gong, H. Z. He, and M. N. Gao, 2017: Characterizing two types of transient intraseasonal oscillations in the eastern Tibetan Plateau summer rainfall. *Climate Dyn.*, **48**, 1749–1768, https://doi.org/10.1007/s00382-016-3170-z.

——, S. Y. Li, T. Zhu, X. Qi, J. P. Liu, S.-J. Kim, and D. Y. Gong, 2022: Intraseasonal melting of northern Barents Sea ice forced by circumpolar clockwise propagating atmospheric waves during early summer. *J. Climate*, **35**, 5703–5718, https://doi.org/10.1175/JCLI-D-21-0538.1.

Yang, L., and Q. Zhang, 2008: Climate features of summer Asia subtropical westerly jet stream. *Climatic Environ. Res.*, **13**, 10–20.

Yang, Q., 2001: The drought/flood in the low reaches of Yang-Tze River and the interannual variations of the 30–60 day oscillation of Eurasian circulation during summer half year. *Acta Meteor. Sin.*, **3**, 318–326.

Yang, S., and T. Li, 2016: Intraseasonal variability of air temperature over the mid-high latitude Eurasia in boreal winter. *Climate Dyn.*, **47**, 2155–2175, https://doi.org/10.1007/s00382-015-2956-8.

——, B. Wu, R. Zhang, and S. Zhou, 2013: The zonal propagating characteristics of low-frequency oscillation over the Eurasian mid-high latitude in boreal summer. *Sci. China Earth Sci.*, **56**, 1566–1575, https://doi.org/10.1007/s11430-012-4576-z.

Zhang, C., 2005: Madden-Julian oscillation. *Rev. Geophys.*, **43**, RG2003, https://doi.org/10.1029/2004RG000158.

Zhong, S., H. Wang, B. Chen, and H. Chen, 2022: Modulation of the atmospheric heat source over the Tibetan Plateau on the intra-seasonal oscillation of summer precipitation in the Yangtze-Huaihe River Basin. *Atmos.–Ocean*, **60**, 600–612, https://doi.org/10.1080/07055900.2022.2077170.

Zhou, S., and A. Miller, 2005: The interaction of the Madden–Julian oscillation and the Arctic Oscillation. *J. Climate*, **18**, 143–159, https://doi.org/10.1175/JCLI3251.1.

Zhou, Y., J. Yuan, Z. Wen, X. Chen, Y. Guo, and X.-Q. Yang, 2023: The influence of the wave trains on the intraseasonal variability of the East Asian subtropical westerly jet in early and late summer. *Climate Dyn.*, **60**, 2081–2095, https://doi.org/10.1007/s00382-022-06412-z.

Zhu, T., and J. Yang, 2021: Two types of mid-high-latitude low-frequency intraseasonal oscillations near the Ural Mountains during boreal summer. *J. Climate*, **34**, 4279–4296, https://doi.org/10.1175/JCLI-D-20-0589.1.

Zhu, Z., and T. Li, 2018: Extended-range forecasting of Chinese summer surface air temperature and heat waves. *Climate Dyn.*, **50**, 2007–2021, https://doi.org/10.1007/s00382-017-3733-7.

Zwiers, F. W., and H. V. Storch, 1995: Taking serial correlation into account in tests of the mean. *J. Climate*, **8**, 336–351, https://doi.org/10.1175/1520-0442(1995)008<0336:TSCIAI>2.0.CO;2.